Verification and Validation of turbulent flow calculations using an adaptive finite-element solver

A. Hay[1] and D. Pelletier[2]

[1] *Industrial Materials Institute, National Research Council Canada, Boucherville, Québec, Canada.*

[2] *Département de Génie Mécanique, Ecole Polytechnique de Montréal, Montréal, Québec, Canada.*

1 Introduction

Accurate and reliable predictions of fluid flows have been the topic of much research over the past decades. A review of the literature reveals that, in many cases, predictions of a given flow by different authors show unexpectedly large scatter. This can be especially disconcerting when people produce vastly different predictions while using similar models and numerical methods. Thus, the question of the error associated to numerical solutions arises to determine to which extent a solution is reliable. Irrespective of the quality of a mathematical model, the accuracy of a numerical procedure or the attention paid to numerical linear solver, an error will always exist. The quantification of this error is of great importance since it ascertains the trust that one can legitimately have in the computed solution. A growing effort has been undertaken by the computational science community to quantify uncertainty in computer simulations. In Computational Fluid Dynamics (CFD) this endeavor has led to a broad discussion on Verification and Validation (V&V) by several organizations such as the AIAA, the ASME, the ERCOFTAC or the ITTC Resistance Committee.

Following, the first two workshops on CFD Uncertainty Analysis, the third edition of this event proposes activities that cover the three essential steps in V&V as discussed in Roache's book [1] : (1) Code Verification; (2) Solution Verification; and (3) Validation. Verification is defined as a synonym for solving the equations accurately (*Solving the equations right*). Hence, Verification is essentially and strictly in mathematical and numerical analysis and performed in two steps. The first one is *Code Verification* which aims at identifying and removing any programming error. Once this step is completed, one can focus on the other types of errors having full confidence in the solver at hand. Furthermore, the effective convergence rate of the numerical methods used is assessed numerically. The Method of the Manufactured Solution (MMS) [2] provides a rigorous framework to easily perform Code Verification. Moreover, the performance of error estimators and reliability of uncertainty estimation procedures can also be evaluated by comparison to true errors. The second step, *Solution Verification*, aims at evaluating the discrepancy between the exact solution to the differential equations modeling the phenomenon of interest and the exact solution to the algebraic equations arising from discretization. When computer round-off and iteration errors can be deemed negligible, Solution Verification reduces to the evaluation of discretization errors. The third step, *Vali-*

dation, is the process of determining if the right equations are solved for the process at hand (*Solving the right equations*). It is essentially and strictly an engineering activity involving comparison with laboratory or field data. It goes without saying that one performs Validation only with *verified simulations* obtained from *verified codes*.

This paper presents and analyzes the results from the workshop activities for the set of numerical techniques developed at the mechanical engineering department of the Ecole Polytechnique of Montréal. As will be shown, numerical predictions and uncertainty analysis all rely on grid adaptation. The paper is organized as follows. Section 2 gives a quick overview of the modeling equations and numerical techniques that are well-established and documented in the literature. Section 3 details the adaptive procedure along with the *tools for Verification and Validation*. These seemingly unrelated topics are presented jointly because they are closely linked together in our approach. Subsection 3.1 focuses on error estimation while subsection 3.2 deals with uncertainty estimates. The next three sections linearly present the outcomes of the three V&V exercises in the mandatory order : Code Verification in section 4, Solution Verification in section 5 and Validation in section 6. Concluding remarks end our report on the workshop activities in section 7.

2 CADYF at a glance

CFD predictions of turbulent flows are computed from the CADYF (Calcul et Analyse en DYnamique des Fluides or *Computer-Assisted DYnamics of Fluids*) flow solver that has been developed over the past 30 years. An up-to-date and detailed presentation of modeling equations and the numerical techniques to solve them can be found in Refs. [3, 4]. This section only summarizes the main ingredients of the CFD approach used for the workshop activities.

2.1 Modeling equations

- The flows of interest are described by the Reynolds-Averaged Navier-Stokes (RANS) equations.
- The system of equations is closed by computing the turbulent viscosity using the standard $k - \epsilon$ model.
- To preserve positivity of the dependent variables (which has several advantages; see Ref. [5]), we work with the logarithms of the turbulence kinetic energy and its dissipation rate. The equations for $\mathcal{K} = \ln(k)$ and $\mathcal{E} = \ln(\epsilon)$ are derived by taking the logarithms of the original equations for k and ϵ. Hence, the turbulence model is unchanged; only the computational variables are different.
- Wall functions are used to describe the solution in the near wall regions. Thus, the computational wall boundary is taken at a distance d from the physical wall boundary. In the gap between the flow is represented by the wall functions.
- We use the two-velocity scale wall functions described by Chabard [6] (see Ref. [3]).

2.2 Numerical techniques

- The resulting system of equations is solved by a finite-element (FE) method that uses a mixed or velocity-pressure formulation. The discretization is based on the Taylor-Hood triangle element (P_2-P_1). That is, the velocity and the logarithmic turbulence variables are discretized using quadratic interpolation functions ($p_{\text{th}} = 3$) and the pressure is discretized by piecewise linear continuous functions ($p_{\text{th}} = 2$).

- To avoid non-physical oscillations in solutions of high Reynolds number flows, the Streamline Upwind/Petrov-Galerkin (SUPG) stabilized formulation is used (see Refs. [7, 8]). It locally introduces small amount of artificial numerical diffusion which may lead to reduced accuracy compared to the standard Galerkin formulation.

- All non-linear algebraic equations are linearized by Newton's method.

- All linear algebraic systems are solved using a sparse direct solver using the Unsymmetric MultiFrontal method (see Ref. [9]).

- The global system of equations are solved in a partly segregated manner (see Refs. [10, 11]).

- An adaptive remeshing procedure driven by the Zhu-Zienkiewicz (ZZ) error estimator is used to yield grid independent numerical predictions (see Section 3.1).

3 Tools for Verification and Validation

3.1 Error Estimation and adaptive procedure

The accuracy of the finite-element approximation can be directly related to the local mesh size. An adaptive remeshing procedure is employed to improve the accuracy, by refining the mesh in regions of high error in the flow and turbulence variables. Regions targeted for refinement are identified by the Zhu-Zienkiewicz (ZZ) error estimator [12, 13] which evaluates estimates of elemental error norms. It has been shown to be asymptotically exact using a proper measure (norm) of the error for a class of elliptic problems. The error estimator is based on local projections of discontinuous quantities onto a local continuous polynomial basis. For example, since the P_2-P_1 element uses a piecewise quadratic basis for the velocity, the stress tensor is linear and discontinuous. By projecting it onto a continuous polynomial basis, we can derive an error estimate defined as the difference between the FE stresses (denoted by the subscript h) and their projections (denoted by the subscript zz). Thus, the elemental error can only be measured in the so-called energy norm (or a mathematically equivalent such as the H^1 semi-norm). As a consequence, the following error norms are considered in the present work :

$$\text{H1U} \quad : \quad ||\mathbf{e_u}||_{H^1} = \sqrt{\int_\Omega (\nabla e_u \cdot \nabla e_u + \nabla e_v \cdot \nabla e_v)\ d\Omega} \tag{1}$$

$$\text{H1P} \quad : \quad ||e_p||_{H^1} = \sqrt{\int_\Omega \nabla e_p \cdot \nabla e_p\ d\Omega} \tag{2}$$

$$\text{EVK} \quad : \quad ||e_{\mathcal{K}}||_{eqv} = \sqrt{\int_{\Omega} \nabla e_{\mathcal{K}} \cdot \nabla e_{\mathcal{K}} \, d\Omega} \tag{3}$$

$$\text{EVE} \quad : \quad ||e_{\mathcal{E}}||_{eqv} = \sqrt{\int_{\Omega} \nabla e_{\mathcal{E}} \cdot \nabla e_{\mathcal{E}} \, d\Omega} \tag{4}$$

$$\text{EVM} \quad : \quad ||e_{\mu_t}||_{eqv} = \sqrt{\int_{\Omega} \nabla e_{\mu_t} \cdot \nabla e_{\mu_t} \, d\Omega} \tag{5}$$

The exact error norms are obtained by considering the difference between the FE fields and their exact counterparts when available (*e.g.* $\mathbf{e_u} = \mathbf{u}_{\text{exa}} - \mathbf{u}_h$). The ZZ estimates are obtained by considering the difference between the FE fields and their projections (*e.g.* $\mathbf{e_u} = \mathbf{u}_{\text{zz}} - \mathbf{u}_h$). The above expressions yield global error norms when integration is performed on the whole domain Ω. Elemental errors and estimates result from integration over a given element volume Ω_k.
Once error estimates are obtained for all variables (flow and turbulence variables), an optimal mesh size distribution is determined using the asymptotic convergence rate of the finite-element method and the principle of equidistribution of the error. The optimal mesh is generated to redistribute the mesh sizes so that each element has the same contribution to the norm of the total error. This is performed in an iterative fashion, beginning with a coarse mesh and producing a sequence of meshes which reduce the error by a constant factor ζ over that of the previous mesh. The mesh characteristics (element sizes) are derived separately for each dependent variable using the norms previously defined. The minimum element size predicted by each of the dependent variable is selected on a given element. The computational domain is then remeshed using an advancing front technique. Details of this adaptive remeshing procedure may be found in the literature [14, 15]. Note that an additional error estimate for the eddy viscosity is also constructed since slowly varying fields of $\mathcal{K}$ and $\mathcal{E}$ can result in rapid variations of μ_t. This is important to the success of adaptation in turbulent flows since the eddy viscosity is the sole mechanism for transfer of momentum and turbulence kinetic energy by turbulent fluctuations [16].

The ZZ error estimator belong to a category of single-grid a posteriori error estimators known as auxiliary algebraic evaluations (AAE). Within AAE, it falls in the family of post-processing techniques (or least-squares-based recovery techniques). In practice, recovery-based estimators perform surprisingly well in estimating error norms (even in cases where no super-convergent property holds). As will be shown and already illustrated in the literature [16, 15], the ZZ estimator is ideally suited for driving mesh adaptation. However, it only yields error estimates in the elemental *norm of the derivatives* and not in quantities of direct engineering interest. This constitutes a serious limitation for Verification and Validation because quantitative assessment of pointwise numerical accuracy is required. To remedy the situation and achieve pointwise error estimates, we proceed as follows. The meshes are generated by adaptive remeshing driven by the ZZ estimator. Error estimates in quantities of engineering interest are obtained by a separate and different reconstruction. We use an L_2 least-squares approach (*i.e.* project the solution rather than its derivatives). We approximate the exact field over an element by a polynomial of degree $k+2$ where k is the degree of the finite-element basis functions. A pointwise error estimate is computed by taking the

difference between the L_2 elemental reconstruction and the finite-element solution in the appropriate element containing the point of interest (see Ref. [17] for details). In what follows, this error estimator will be referred to as the Wiberg estimator.

3.2 Uncertainty prediction within solution adaptation

The accuracy of the ZZ and Wiberg estimators in terms of exact error predictions will be investigated in what follows using the manufactured turbulent flow problem (for which exact solutions and thus true errors are available). Previous experiences from the authors [3] shows that they provide almost *asymptotically exact* error norm estimations (efficiency indexes tend to a value close to one as grid cell sizes tend to zero) and yield the magnitude of the error for pointwise quantities but can not predict any significant digit. However, regardless of their efficiency, they both provide error estimates and not uncertainty predictions. For the present study, we ultimately need 95% certainty error bars (U_{95}) for Validation exercices as well established in the literature and specified in the workshop instructions.

The most widely used numerical uncertainty procedure is the well-known Grid Convergence Index (CGI) proposed by Roache [1]. It is based on Richardson extrapolation which is extremely sensitive to noise in the data that originates from a number of causes. The Least Squares CGI by Eça and Hoekstra [18, 19] partially alleviates this problem but the method still suffers from irregularities in the refinement ratios between meshes in grid convergence studies. Thus, the GCI procedures are limited to sets of geometrically similar grids and hence unsuitable for adaptive grid calculations. In the case of adaptive remeshing, as opposed to local mesh adaptation, this is even true for the last cycles of adaptation for which error equidistribution has converged (so that almost uniform refinement is performed over the computational domain). Regardless of the uniformity of the adaptation, there is no guarantee (and actually little chance) that the mesh topology will be preserved from one cycle to the next by the automatic mesh generator.

As suggested in Ref. [20], uncertainty predictions may be derived from AAE by applying a factor of safety F_s to error estimates. Roache and Pelletier highlight that some $F_s > 1$ always is necessary even when using highly refined adapted grids, no matter how accurate is the solution. Clearly, we agree with this principle since even when ZZ and Wiberg estimators yield sharp error predictions, they are *not* consistently conservative. As a matter of fact, they usually underestimate true errors. Now, evaluation of an adequate factor of safety is not a straightforward task and would require to examine a statistically significant number of cases. In Ref. [20], and references cited therein, it is reported that an efficient adaptive grid strategy may be so effective that the finest grid resolutions always correspond to a required $F_s < 1.25$. On the other hand, for 95% certainty error bars on the coarse grids obtained during the initial stages of the grid adaptive process, the required F_s is sometimes above 3. Based on our experience in the framework of turbulent flows, the range of possibilities for the safety factor is even larger since (1) we report efficiency indexes close to one for global quantities (*i.e.* resulting from integration over the whole computational domain) so that again F_s should be lower than 1.25; (2) we report error estimates that only give the magnitude of the exact error for pointwise quantities suggesting $F_s = 10$!

However, the solution-adaptive ZZ approach offers another error estimator : the difference e between the last two meshes in the adaptive cycle as mentioned in Refs. [20] and [21]. Once

again, we face the tedious issue of deriving a factor of safety. Nevertheless, our previous experiences indicate that $F_s = 3$ may be an appropriate choice to achieve 95% certainty. This conjecture will be confronted here to the data for which true errors are available to test the adequacy of the correlation of $F_s = 3$ with U_{95}. We do *not* pretend that this is sufficient to allow for a definite conclusion and clearly much more subsequent testing is required to access this uncertainty prediction procedure (once again on a statistically significant number of cases). However, should it provide reliable uncertainty estimates, it would be yet another powerful feature of mesh adaptivity. To summarize, following the notation in the workshop validation procedure, we have :

$$U_{\text{num}}(f) = F_s \mathtt{e} \quad \text{with } \mathtt{e} = |f_2 - f_1| \text{ and } F_s = 3, \tag{6}$$

where f_1 and f_2 are the solutions predicted on the last two adapted grids.
Obviously, the reliability of this grid-adaptivity based uncertainty prediction approach crucially depends on the mesh adaptation procedure itself. To our beliefs, the following points is a non-exhaustive list of requirements :

1. Mesh adaptation must be driven by an ordered error estimator and not merely an error indicator (though such adaptive procedures may be effective for improving solution accuracy).

2. All dependent variables must contribute to the error that drives mesh adaptation and mesh characteristics (element sizes) must be based on the minimum mesh size predicted over all variables.

3. Reliability may not be observed for the very first adaptive cycles. That is, sufficient refinement steps may be necessary for the difference between two solutions to be indicative of an error estimate.

4. The error reduction factor ζ (see Section 3.1) must be kept constant during the whole adaptive process. Furthermore, its value is related to the safety factor F_s in Eq. 6. Indeed, our empirical choice of $F_s = 3$ only is valid for $\zeta \in [0.6, 0.8]$. Other values would increase or slow the convergence rate on successive grids making the $\mathtt{e}$ error estimate more or less conservative respectively. Note that the error reduction factor is always chosen in this range because it brings about the best performance out of the adaptive process. Smaller values may lead to strong and possibly inadequate refinement due to inaccurate error estimations (adaptation not only improves the accuracy of the solution but also the error estimator which in turns allows for better mesh adaptation). On the other hand, larger values generally lead to excessively slow adaptive processes.

4 Code Verification by the MMS

The first workshop exercise is Code Verification by the Method of the Manufactured Solution (MMS) [1, 2, 22]. Since all numerical solutions are produced through an adaptive FE code, we have to verify the flow solver, the error estimators and the adaptive process. We also take the opportunity to have a closed-form solution to assess the reliability and accuracy of the error estimators for global and local estimates as well as for uncertainty predictions.

4.1 Manufactured solution and Boundary conditions

The manufactured solution mimics the near-wall behavior of a two-dimensional, steady incompressible turbulent boundary-layer. The near-wall behavior of all the specified quantities is similar to what is observed in near-wall turbulent flows. The Reynolds number is set to one million. The manufactured solution variables and the source terms defining the modified problem are described in details in Ref. [23]. Additional source terms are required for verification of wall functions as detailed in Ref. [24]. Compared to what is described in Ref. [23], we have to slightly modify the Manufactured Solution to fit our computational approach where the computational variables for the turbulence model are the logarithms of k and ϵ. We have added small constants α_k and α_ϵ to the manufactured variables k and ϵ to avoid logarithms of zero values.

$$k = k_{max}\eta_\nu^2 e^{1-\eta_\nu^2} + \alpha_k, \tag{7}$$

$$\epsilon = 0.36\frac{k_{max}^2}{\nu_{max}} e^{-\eta_\nu^2} + \alpha_\epsilon, \tag{8}$$

A trade-off must be made when choosing the values of the two constants : they must be large enough to avoid any numerical problem originating from the logarithm function; they must small enough so that the differences with the original manufactured solution is negligible (including the manufactured eddy-viscosity field). Following these observations, we have chosen [3] :

$$\alpha_k = 10^{-5} \quad ; \quad \alpha_\epsilon = 10^{-3}. \tag{9}$$

The analytical solution for all variables is imposed on the inflow (as required by the workshop instructions) and upper boundaries as Dirichlet boundary conditions. On the outlet, the normal and tangential forces on the boundary are imposed from the exact velocity and pressure fields. The diffusion fluxes of k and ϵ are also imposed from the manufactured solution. Hence, on the outlet Neumann boundary conditions are applied on all variables.
On the wall, the workshop instructions require to impose Dirichlet boundary conditions. Such a setting is suited to perform Code Verification for turbulence models with low-Re formulations. However, this is not adequate for a complete Code Verification procedure for our computational framework. Indeed, we need to verify the wall-function implementation along with the other typical boundary conditions used for addressing turbulent flows. Thus, we consider a first case where manufactured wall-functions are used at the bottom boundary. The type of boundary conditions is determined according to the wall functions :

- u : Robin boundary condition
- k : Neumann boundary condition
- v : Dirichlet boundary condition
- ϵ : Dirichlet boundary condition

As described in Refs. [24], source terms are added in the standard wall-functions boundary conditions to ensure compatibility with the manufactured solution (*i.e.* all imposed BC values are determined from the manufactured solution variables). The wall distance is set to $d = 0.006$ to ensure, for a Reynolds number of one million, that the non-dimensional wall distance d^+ lies in $[30, 300]$ on all walls remaining as close as possible to 30 for improved accuracy. This first setting allows for Code Verification of the complete solver for practical turbulent flow problems.
However, we have not followed the workshop instructions for wall boundary conditions. Furthermore, the verification procedure requires to examine local flow quantities at two near-wall locations for which $y < 0.006$ ($y = 0.001$ and $y = 0.002$). Hence, they are located in the gap between the physical wall ($y = 0$) and the computational wall ($y = d$) where solution

variables are not solved but defined according to the manufactured (*exact*) wall functions. Here, it means that the exact manufactured solution variables are used so that no error can be reported at these locations. This merely is an artifact of the wall-function modeling. To circumvent this limitation, we consider a second case for which manufactured Dirichlet boundary conditions are used at the bottom boundary for all variables. Hence, equations are integrated down to the physical wall ($y = 0$) following what is done when low-Re modeling is used. Thus, wall functions are deactivated and not part of the verification exercise. We will use this second case to report results on local flow quantities. We emphasize that the manufactured eddy-viscosity are not exactly zero at the wall, as opposed to what is described in Ref. [23], since we have added small constants α_k and α_ϵ to the manufactured turbulence variables.

4.2 Numerical results

4.2.1 First Case : with wall functions

This first configuration allows for a complete Code Verification. We will report here observed orders of accuracy on all variables as well as results on the friction resistance as it would be the case for practical applications.

Eight grid adaptation cycles have been performed, the last adapted grid (# 8) contains 462,338 nodes. Figure 1 shows the grid # 6 which has 135,460 nodes (the last two grids being too fine to be of any visual interest). It is typical of adapted meshes for boundary layer flow problems as expected. Extensive refinement is observed in the near-wall region. Several bands of refinement can also be identified which correspond to regions of rapid variation in velocity, $\mathcal{K}$, $\mathcal{E}$ and μ_t.

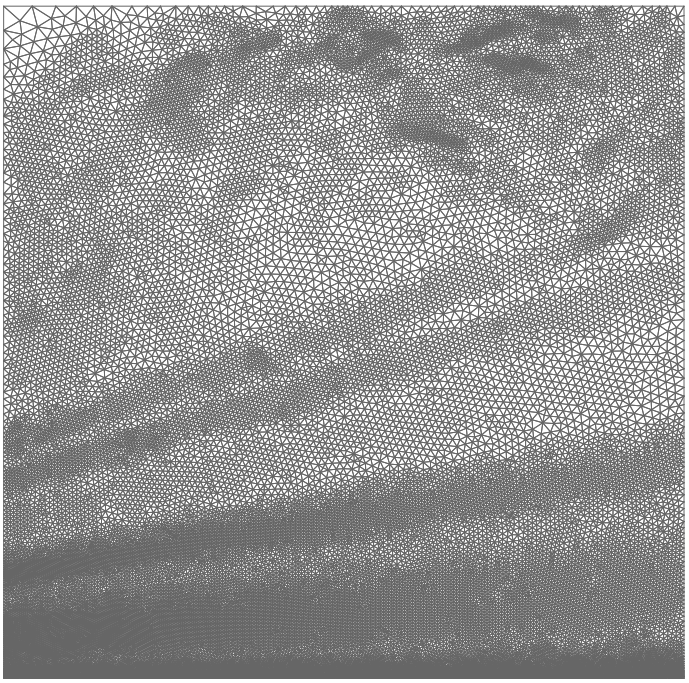

Figure 1: 6^{th} adapted mesh for the MS with wall functions

We first check that the non-dimensional wall distance y_+ lies in the interval of validity

imposed by the wall functions. We have chosen the distance d based on the manufactured solution fields to enforce that $y_+ \in [30, 300]$ and remains close to 30. Note that since we use a manufactured solution, this condition is not necessary as opposed to real flow problems. Figure 2 shows the distribution of y_+ along the bottom boundary. As can be seen, the condition is fulfilled as expected from our construction.

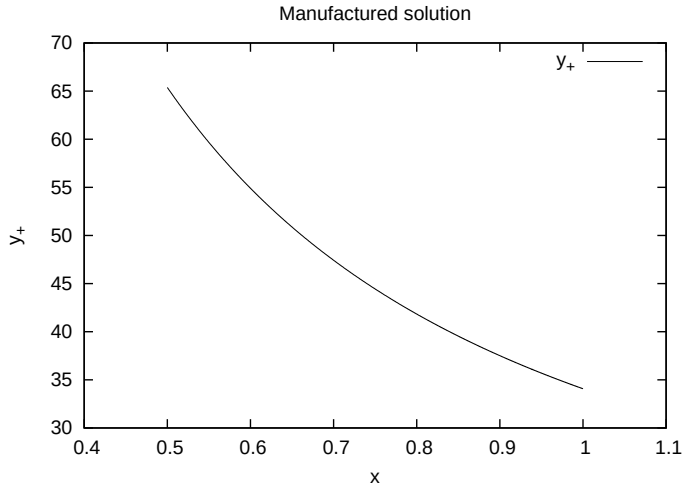

Figure 2: Distribution of y_+ along the bottom boundary

Figures 3 and 4 shows the evolution of the global error norms defined by Eqs. (1) - (5) (true and estimated) with the adaptive cycles. The corresponding efficiency indexes (ratio of estimated error over the exact error, *e.g.* $\xi_{\mathrm{H1U}} = ||\mathbf{e_u}||^{\mathrm{zz}}_{H^1} / ||\mathbf{e_u}||^{\mathrm{exa}}_{H^1}$) are presented in figure 5. As can be seen, the errors decrease with mesh refinement and the numerical solution converges towards the exact solution. Furthermore, the error estimates approach the true errors with mesh refinement. This indicates that adaptation improves the accuracy of both the solution and the error estimator. Table 1 gives the values of the global error norms along with their

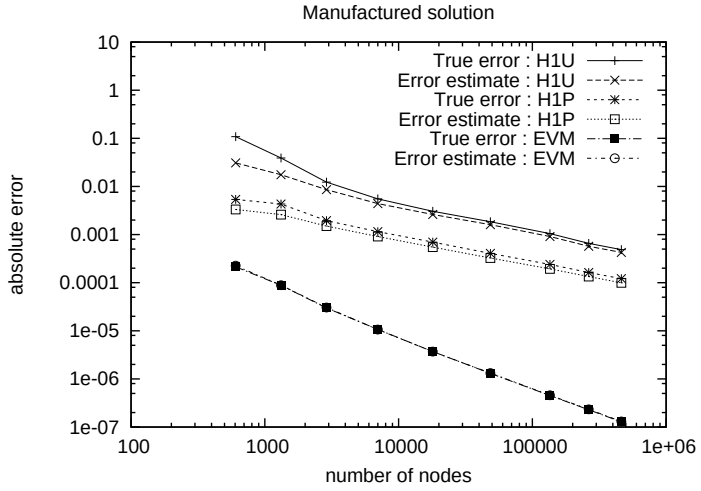

Figure 3: Evolution of global error norms with adaptive cycles (1)

associated efficiency indexes computed on the last adapted mesh. As can be seen, all the

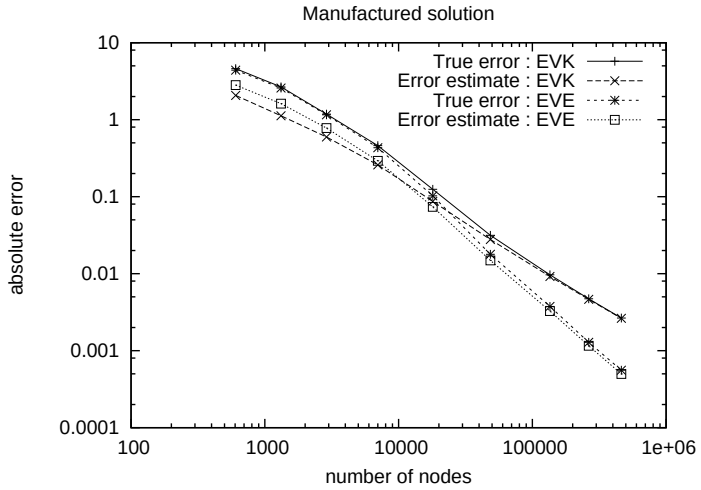

Figure 4: Evolution of global error norms with adaptive cycles (2)

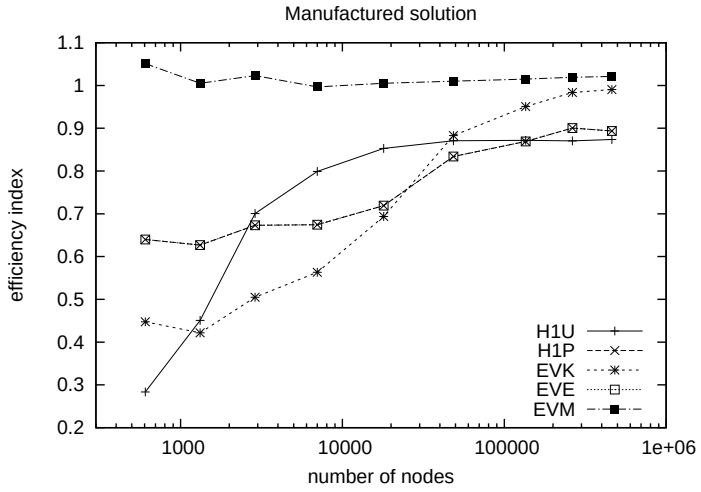

Figure 5: Evolution of efficiency indexes with adaptive cycles

efficiency indexes are close to one indicating that the ZZ error estimator performs well.

	Exact	Estimated	Efficiency index
H1U	$4.854\,10^{-4}$	$4.242\,10^{-4}$	0.874
H1P	$1.211\,10^{-4}$	$9.966\,10^{-5}$	0.823
EVK	$2.656\,10^{-3}$	$2.631\,10^{-3}$	0.990
EVE	$5.570\,10^{-4}$	$4.978\,10^{-4}$	0.894
EVM	$1.284\,10^{-7}$	$1.310\,10^{-7}$	1.021

Table 1: Global error norms

As part of the Code Verification exercise, we now look at the observed orders of conver-

gence for the dependent variables. They are computed from the reductions of the true global error norms between two consecutive meshes assuming that the asymptotic range is reached. However, the use of the adaptive procedure leads to a difficulty in the evaluation of these orders since the refinement ratio between two consecutive adaptive grids is generally not uniform over the computational domain especially during the first cycles. Uniform refinement is only observed when the asymptotic range has been reached and the error equidistribution has converged. It might be true for the last adaptive cycle (given that the adaptive grid # 7 already has more than 260,000 nodes) but certainly not for the previous ones. In order to obtain a set of geometrically similar grids, we start from the finest adaptive grid (# 8) and apply a refinement ratio of 1/2 to generate coarser grids. This is equivalent to a coarsening by $\sqrt{2}$ in each direction so that the number of grid points is halved at each cycles of mesh coarsening. This is easily done by our advancing front mesh generator but can not be enforced exactly everywhere for technical reasons. However, the refinement ratio between two consecutive meshes is nearly constant over the domain.The observed rates of convergence (computed from true error norms) for all variables are given in table 2. Without the stabilization terms, the theoretical orders of accuracy of the standard Galerkin FEM should be 3 for all variables but the pressure for which the order should be 2. However, the stabilization formulation locally introduces some amount of artificial numerical diffusion which degrades the accuracy. The exact amount of diffusion introduced is problem dependent so that we can only expect the observed orders to be between 1 and 3 (except for the pressure for which it should be between 1 and 2). Indeed, it is impossible to foretell what is the amount of artificial diffusion arising from the stabilization formulation. The only established fact is that it clearly depends on the Reynolds number. As can be seen in table 2, the convergence rates for p, $\mathcal{K}$ and μ_t are close to their *best* theoretical counterparts (stabilization has almost no effect on their observed orders of convergence). For the velocity variable, the observed order of convergence is close to the lowest limit of its theoretical range. This means that the effect of the stabilization terms is more pronounced on the velocity than on the other variables. However, the stabilization terms also act on $\mathcal{E}$ since its convergence rate is too large which means that its error reduction with mesh refinement is too fast. Note that similar conclusions

	$\mathbf{u}$	p	$\mathcal{K}$	$\mathcal{E}$	μ_t
grid 8/7	2.089	2.063	3.056	3.766	3.062

Table 2: Observed orders of convergence on solution variables

are drawn from the observed orders of convergence calculated using the last two adapted grids so that the use of the uniformly coarsened grids was unnecessary. As to the Code Verification exercise, this result on the $\mathcal{E}$ rate of convergence is cumbersome since full Verification requires that observed orders of convergence for all variables to converge to some limits inside their theoretical ranges. However, the convergence of the efficiency indexes with mesh refinement in fig. 1 leaves little room for any programming error in the flow solver. Indeed, even the slightest error in the code would prevent such a clear-cut convergence behavior. Hence, we are confident that this result for the $\mathcal{E}$ variable is due to the stabilization formulation. The upwinding it introduces somehow leads to an observed order of convergence higher that the degree of the FE interpolation functions.

We now focus on the evaluation of the accuracy of the error estimation technique for an integral engineering quantity : the friction resistance C_f on the bottom wall. Taking $\rho U_{\text{ref}}^2 L_{\text{ref}}$

as a reference force, the friction resistance is computed as follows :

$$C_f = \frac{1}{\rho U_{\text{ref}}^2 L_{\text{ref}}} \int_{\Gamma_w} \tau \cdot \hat{\mathbf{n}} \cdot \mathbf{e_x} \, d\Gamma = \frac{1}{U_{\text{ref}}^2 L_{\text{ref}}} \int_{\Gamma_w} (\nu + \nu_t) \left(\frac{\partial u}{\partial y} + \frac{\partial v}{\partial x} \right) \, d\Gamma. \tag{10}$$

When the near-wall behavior is determined from a low-Re formulation, integration is performed down to the wall so that ν_t and $\frac{\partial v}{\partial x}$ are zero at the bottom boundary (for a flat wall aligned with the x-axis). Here, we report a friction coefficient calculated at the computational bottom boundary where the wall-functions apply. Thus, the integrand in Eq. (10) can not be reduced to the normal derivative of the streamwise velocity component times the molecular viscosity. Recall also that the manufactured ν_t is slightly affected by the additional α_k and α_ϵ constants in the manufactured turbulence variables used to prevent logarithms of zero values. Also, the friction resistance could have been calculated using the law of the wall function. Figure 6 shows the evolution of the friction resistance with adaptive cycles. As can be seen, a clear grid convergence of C_f is achieved by the adaptive strategy. Figure 7

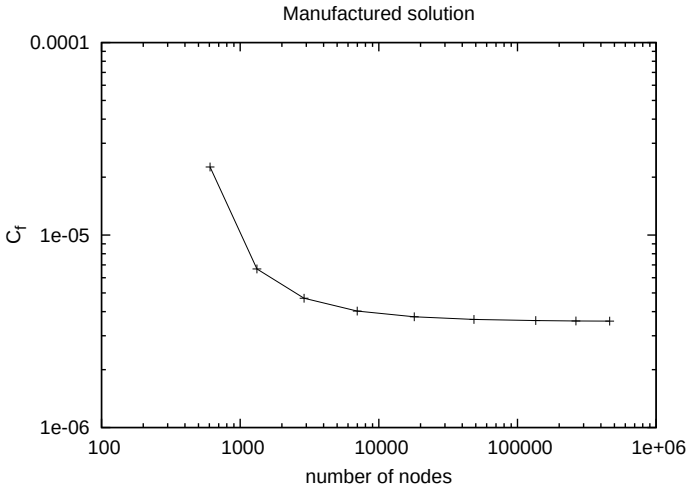

Figure 6: Evolution of C_f with adaptive cycles

shows the corresponding evolution of the true and Wiberg estimated errors. It confirms that the error on the friction coefficient is reduced at each adaptive cycle. Furthermore, the error estimates converges to the true error surprisingly well with its efficiency index close to one for the last adapted cycles. This is in contrast with the results obtained during the second workshop where error estimations on integral quantity was reported to provide only the order of magnitude of the error but was unable to predict any significant digit. Note that the error estimation procedure is unchanged but we used much finer grids that two years ago and the bottom wall is located at the different position as explained previously. However, though the efficiency index can be made as close to one as desired, we note that it converges from the lower side. That is, similarly to the estimated error norms from the ZZ estimators, the efficiency indexes are lower than one. This means that true errors are under-predicted which makes the estimators non-conservative and further stresses the need for the application of a safety factor to yield reliable uncertainty predictions.

Figure 8 shows the error bars for C_f with adaptive cycles as predicted by our uncertainty estimate U_{num} given by Eq. (6). These error bars are compared with the true error bars. As can be seen, the error bars from the uncertainty estimation procedure all overlap the

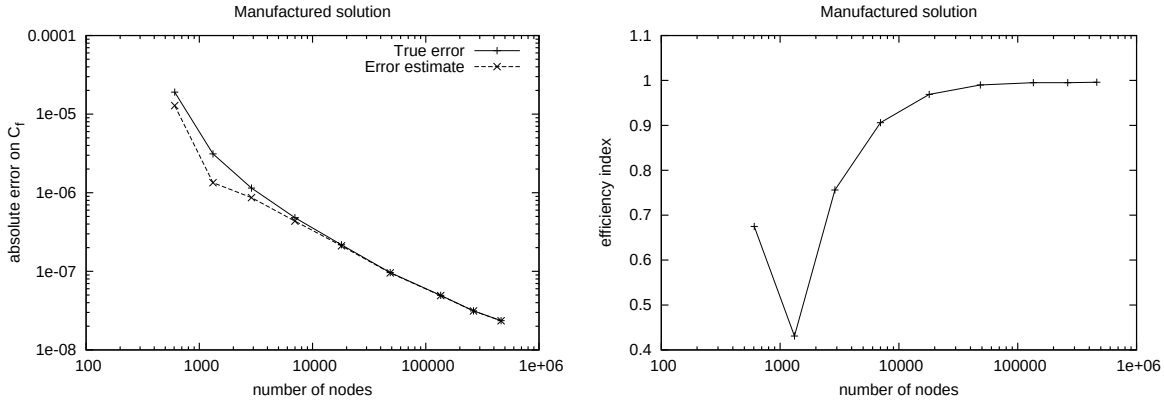

(a) Errors on C_f (b) Efficiency index

Figure 7: Evolution of error estimates on C_f with adaptive cycles

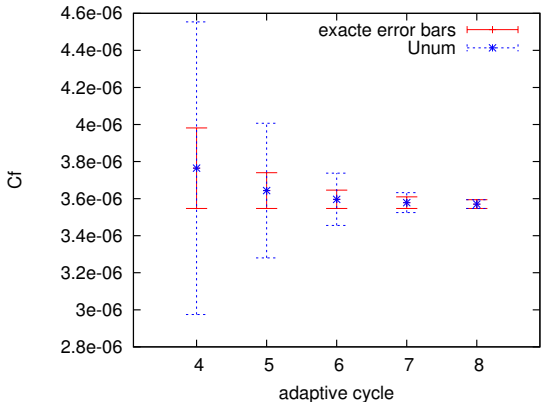

Figure 8: Error bars for C_f with adaptive cycles

true error bars. Also, the predictions gets closer and closer to the true error bars with mesh refinement.

4.2.2 Second Case : without wall functions

This second configuration is used to report results on pointwise quantities as explained in Section 4.1. Here, the bottom boundary is located at $y = 0$ and corresponds to the physical flat wall so that Dirichlet boundary conditions are applied on all variables. Wall functions are not used and thus not tested. Again, eight grid adaptation cycles have been performed, the last adapted grid (# 8) contains 516,078 nodes. It is very similar to the one presented above.

The accuracy of the error estimation technique for local flow quantities is now examined. The coordinates of the three local points under consideration are : Point 1 (0.600,0.001), Point 2 (0.750,0.002) and Point 3 (0.900,0.200). At these locations, we study the values of the velocity components (u and v), the pressure coefficient C_p, the eddy-viscosity ν_t and their associated errors. Note that here, the pressure coefficient is defined as :

$$C_p = \frac{p}{\rho U_{\text{ref}}^2}. \tag{11}$$

The results are collected in table 3. The quality and reliability of the error estimator on point-

Local point	Variables	Value	Exact Error	Estimated Error	Efficiency index
1	u	$0.752241\,10^{-2}$	$0.102\,10^{-7}$	$0.879\,10^{-8}$	0.861
	v	$0.626537\,10^{-5}$	$0.326\,10^{-8}$	$0.305\,10^{-8}$	0.936
	C_p	$0.961490\,10^{-2}$	$0.248\,10^{-9}$	$0.420\,10^{-9}$	1.694
	ν_t	$0.749295\,10^{-9}$	$0.983\,10^{-14}$	$0.967\,10^{-14}$	0.984
2	u	$0.120356\,10^{-1}$	$0.231\,10^{-7}$	$0.313\,10^{-7}$	1.357
	v	$0.160299\,10^{-4}$	$0.172\,10^{-7}$	$0.103\,10^{-7}$	0.596
	C_p	$0.191728\,10^{-1}$	$0.156\,10^{-8}$	$0.745\,10^{-9}$	0.477
	ν_t	$0.209202\,10^{-8}$	$0.358\,10^{-13}$	$0.450\,10^{-13}$	1.258
3	u	$0.791275\,10^{+0}$	$0.238\,10^{-6}$	$0.283\,10^{-6}$	1.189
	v	$0.770415\,10^{-1}$	$0.194\,10^{-6}$	$0.198\,10^{-6}$	1.020
	C_p	$0.161491\,10^{-1}$	$0.398\,10^{-6}$	$0.351\,10^{-6}$	0.882
	ν_t	$0.676009\,10^{-4}$	$0.285\,10^{-9}$	$0.212\,10^{-9}$	0.746

Table 3: Results for local flow quantities

wise quantities are similar to what was reported two years ago during the second workshop on uncertainty analysis. Actually, this is exactly the same exercise using the same manufactured solution and extracting local values at the same locations. The error estimate based on the Wiberg solution reconstruction over an element predicts the order of magnitude of the exact error for all variables but fails to provide any significant digit of the true error. All in all, error predictions are better that two years ago because efficiency indexes are closer to one. This is probably due to the fact that the final adapted mesh is much finer than the one used during the second workshop. Again, the error estimations are clearly not always conservative

and true errors are under-predicted in a number of cases.

Figures 9 to 11 shows the estimated and true error bars for those local quantities. As can be seen, the adaptivity-based uncertainty estimation procedure performs well in providing reliable error bars in more than 95% of the case. Actually, among the 81 values reported, failure is only observed for the pressure coefficient calculated at the third location on grid # 6. As a general trend, the uncertainty predictions get sharper with respect to the true error bars with the adaptive cycle but this is not always true.

4.3 Conclusions from the Code Verification exercise

- The adaptive procedure driven by the ZZ error estimator has been verified. It has built confidence that the adaptive process automatically yields grid-independent results so that grid refinement studies can be performed with minimum user intervention.
- Results from the grid refinement study all indicate successful Code Verification with the exception of the observed order of convergence for ϵ. We believe it originates from the stabilization formulation which already affects the observed order of convergence for the velocity. However, we have no complete proof supporting our conclusion.
- The ZZ error estimator for global error norms has been demonstrated to be almost asymptotically exact.
- The Wiberg error estimator for quantities of engineering interest only provides the order of magnitude of the error. This is not considered as a poor result given how perform most of error estimators for pointwise quantities (for non-linear and non-elliptic problems).
- Both AAE error estimators usually under-predict the true errors. Hence, a safety factor must be applied to convert any of them into 95% certainty error bars. We don't have sufficient empirical evidences from previous experiences to fix the factor value (we usually only report error estimations from them).
- The adaptivity-based uncertainty estimation procedure has been reliable in more than 95% of the cases examined during the Code Verification exercise. It corroborates previous experiences. However, the error predictions may be over-pessimistic though this tendency seems to be less pronounced when sufficient adaptive cycles have been performed.
- In the light of these results, the next workshop activities will be performed using the adaptive procedure driven by the ZZ error estimator to bring solution predictions while uncertainty bars will be estimated from Eq. (6).

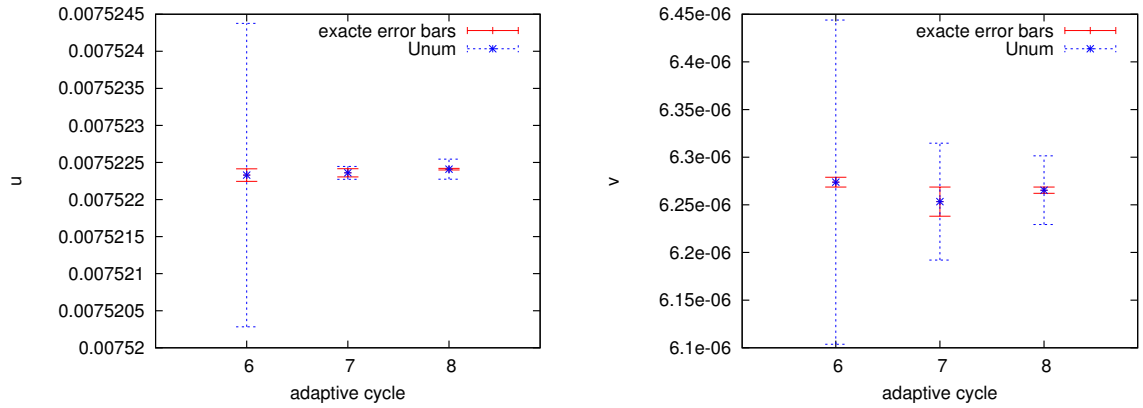

(a) u

(b) v

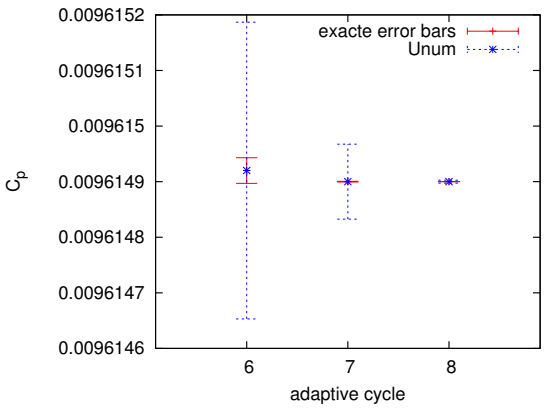

(c) C_p

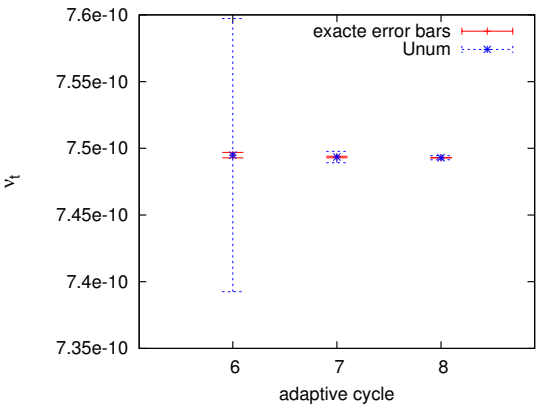

(d) ν_t

Figure 9: Error bars on local quantities (point 1)

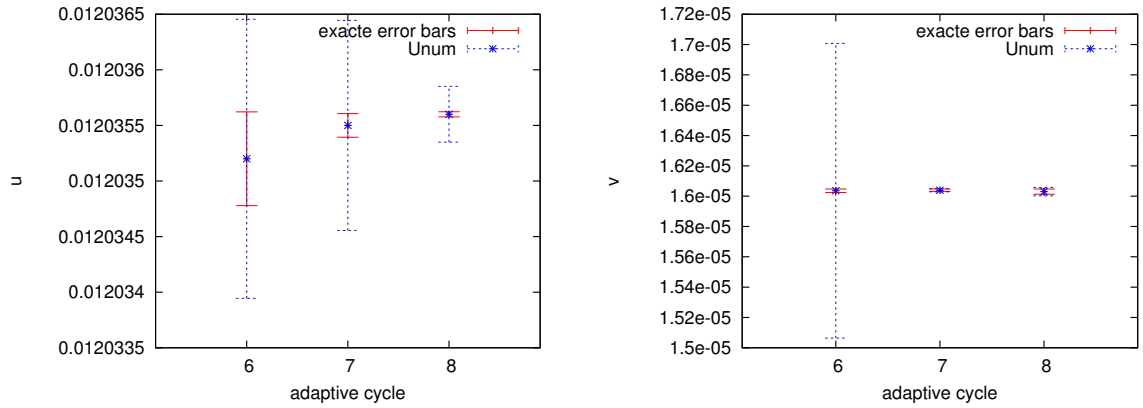

(a) u

(b) v

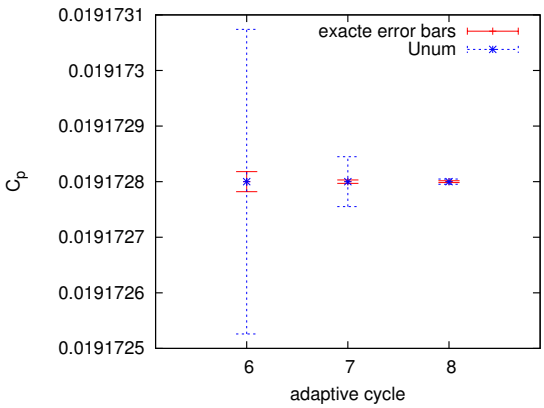

(c) C_p

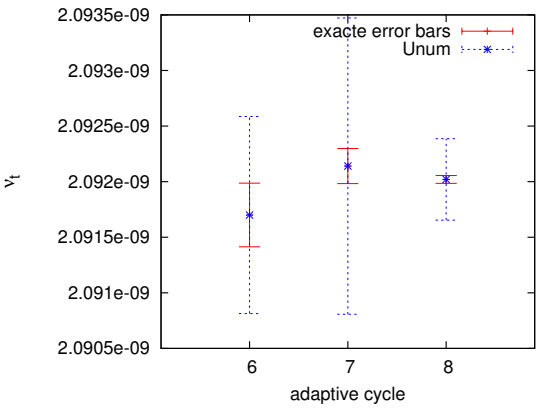

(d) ν_t

Figure 10: Error bars on local quantities (point 2)

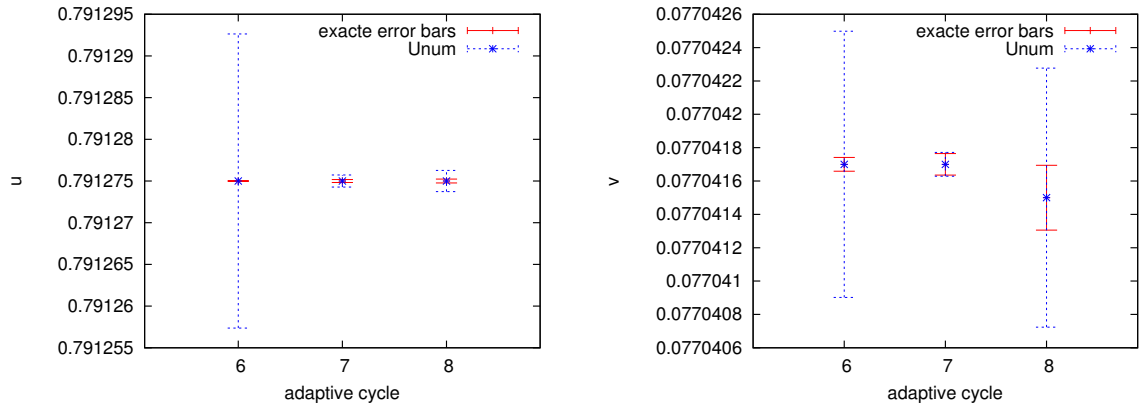

(a) u

(b) v

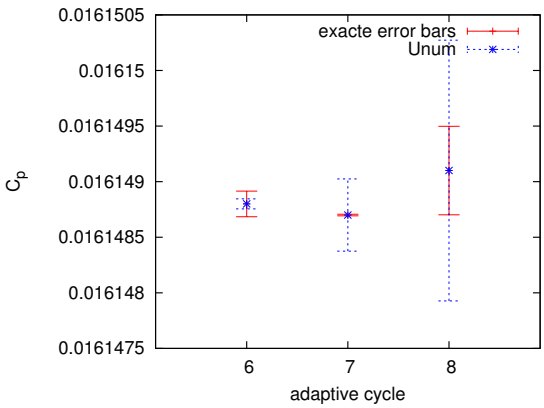

(c) C_p

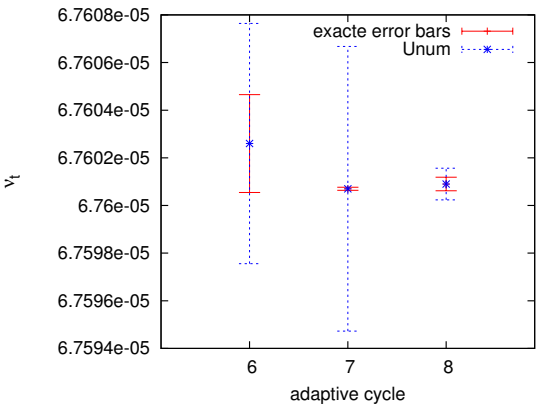

(d) ν_t

Figure 11: Error bars on local quantities (point 3)

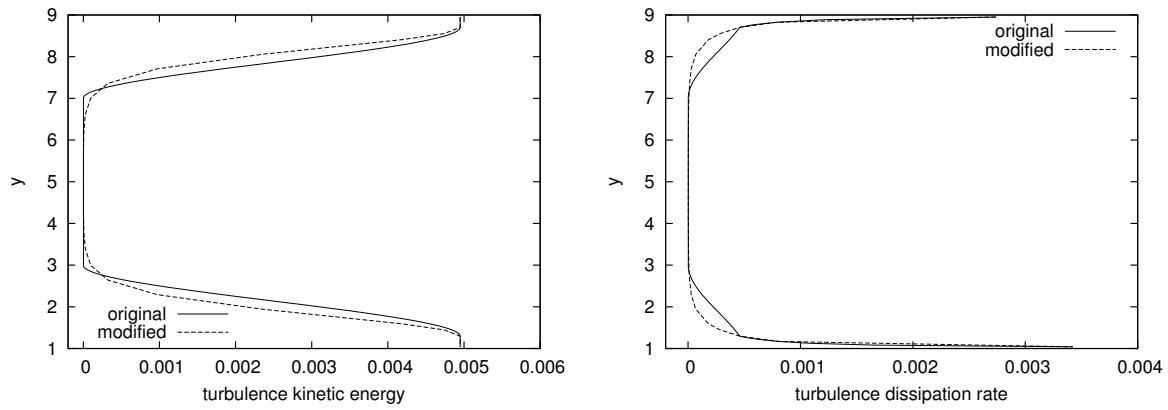

(a) Inlet profiles for k

(b) Inlet profiles for ϵ

Figure 12: Inlet profiles for the turbulence variables

5 Solution Verification for the Backward Facing Step problem

5.1 Test Case description

We now consider the ERCOFTAC C-30 test case : a backward facing step problem at $\mathsf{Re} = 50,000$. The boundary conditions along walls are prescribed using wall functions. At the inlet, Dirichlet boundary conditions are applied and at the outlet we prescribed homogeneous natural FE boundary conditions (Neumann). The inlet profiles for all variables are defined using experimental data and mathematical treatments to ensure the continuity of both the variables and their derivatives. The original inlet profiles for the turbulent variables are plotted in figure 12. As stated, these profiles are constructed in a piecewise manner to obtain C^1 continuous functions as required by most numerical techniques. However, the logarithms of these C^1 continuous functions are not C^1 continuous. This may lead to numerical difficulties for our code. Hence, we sightly modified the inlet profiles. The background experimental data are unchanged but the piecewise mathematical treatment for obtaining the profiles is done so that our computational variables (the logarithms of the turbulent variables) are C^1 continuous. The resulting inlet profiles obtained are plotted in figure 12. We believe that these modifications will only have minor influences on the computed solution since the physic behind them is the same than for the original profiles. Only, the mathematical assembly is different.

5.2 Solution Verification

Thirteen grid adaptation cycles have been performed and the last adapted grids has 489,969 nodes. Similarly to the manufactured solution case, the two last meshes are so fine that it is impossible to distinguish one node from the next when displayed in a figure. Thus, figure 13 shows the grid obtained after 11 adaptive cycles. It *only* contains 131,205 nodes but the main regions of refinement chosen by the error estimates during adaptation can clearly be seen. A close-up view around the step is also provided in figure 14. Similarly to other wall-bounded flow meshes, grid refinement has been performed in the near-wall region of the top and bottom walls. Also, intensive refinement has occurred around the upper corner of the step in the form of two layers of refinement to capture the rapid variations of the flow in this area. This is typical of adapted meshes for backward facing step flows. The adaptive procedure also has

clustered grid points in two different bands that originate from the large curvatures in the inlet profiles for k and ϵ (see fig. 12). These large curvatures in the turbulence variables intensify as they are convected further downstream so that grid cell sizes become smaller and smaller as they get closer to the outlet. Such a pronounced refinement in these areas may seem irrelevant and useless when one is only interested in computing engineering quantities such as the friction or pressure coefficient on walls. However, it clearly illustrates that the essence of adaptivity is to yield solutions with equal accuracy all over the computational domain from the principle of error equidistribution. Such a property is responsible for the general-purpose nature of an adaptive procedure that can thus be confidently applied to any problem regardless of its own specificities.

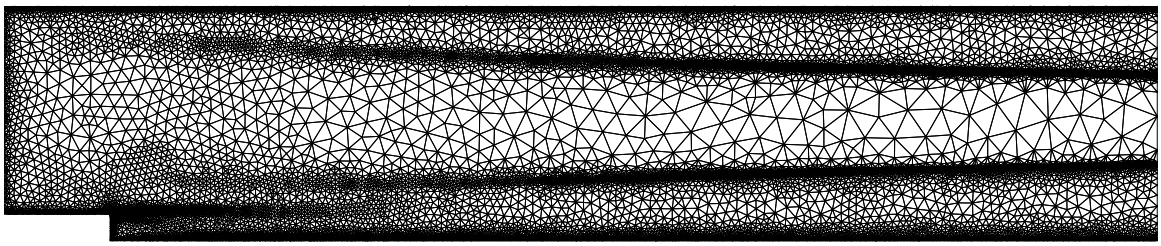

Figure 13: Adapted mesh for the backward facing step

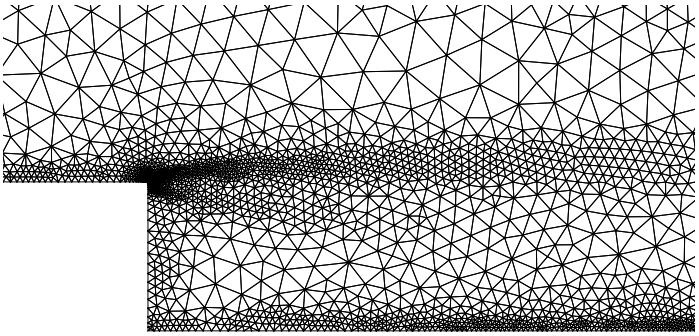

Figure 14: Inside view of the adapted mesh around the step

As part of the Solution Verification exercise, figure 15 shows the evolution of the global error norms with adaptive cycles as predicted by the ZZ estimators. Table 4 gives the observed orders of convergence on solution variables. Note that, as opposed to what has been done for the manufactured problem, we here measure the pressure error in L_2 norm. As can be clearly seen, a grid-converged behavior is reached for all variables. Furthermore, the observed orders of convergence are all in their expected theoretical range so that we conclude the asymptotic range is reached for all variables (at least for such a global measure of the error). This is in contrast with previous results for the manufactured solution case. It is unclear to the authors why the observed behaviors of the convergence of the dependent variables is closer to the theory here. It might be due to a much lower Reynolds number for this case ($\mathsf{Re} = 5\,10^4$) than for the manufactured problem ($\mathsf{Re} = 10^6$) so that the effects of the SUPG stabilization formulation are milder. Note however that this conclusion may not hold for pointwise quantities. That is, this behavior is here observed for global error norms for which integration over the domain may provide an averaging process responsible

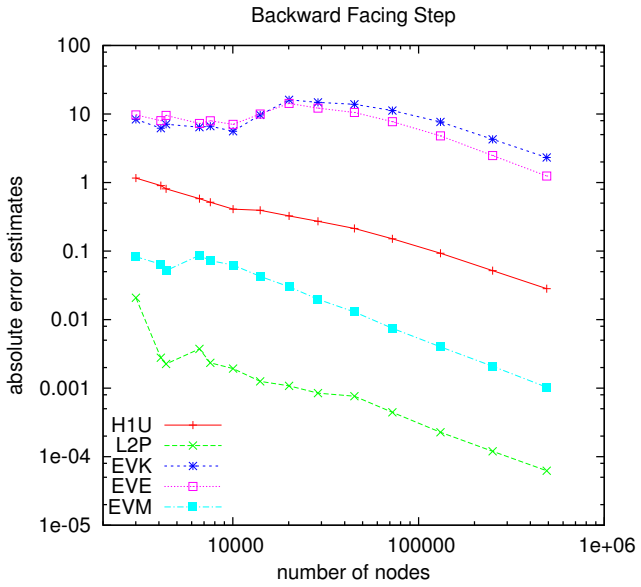

Figure 15: Estimated error norm trajectories

	$\mathbf{u}$	p	$\mathcal{K}$	$\mathcal{E}$	μ_t
grid 13/12	2.800	1.953	2.820	3.049	3.101

Table 4: Observed orders of convergence on solution variables from error estimates

for *smoothing* the observed behaviors. This is the authors' intuition based on heuristics and we do *not* pretend it can be stated as a general result. Finally, one may be surprised by the initial error trajectories for the turbulent variables since these errors increase during the early steps which violates the error reduction target in the adaptive procedure. This is due to poor error estimations on these coarse grids for which the number of nodes is lower than $20,000$.

Before proceeding with any analysis of the results, we must check that the non-dimensional wall distance chosen for each wall lies in the interval of validity imposed by the wall functions. That is, it is required that y_+ is less than 300 and greater than 30 but preferably as close to 30 as possible. Figure 16 gives the evolution of y_+ with adaptive cycles for each wall. As can be seen, the wall distances converge with the adaptive cycles. And, for the last adapted grid, the above condition is satisfied everywhere except near the corner singularity.

We now turn our attention to the quantities of interest for this workshop. We first examine the result for the recirculation length. Figure 17 shows the evolution of the computed recirculation length with adaptive cycles. As can be seen, grid convergence is clearly achieved. The value of the non-dimensional recirculation length computed on the last adapted mesh is 5.4658759. The evaluation of the uncertainty from Eq. (6) is $U_{num}(L_{\text{rec}}) = 0.0015D$. Thus, we report that $L_{\text{rec}}/D = 5.4659 \pm 0.0015$.

We now examine several integral quantities : the friction resistance on the bottom wall $(C_f)_b$ (fig. 18) and the top wall $(C_f)_t$ (fig. 19) and the pressure resistance $(C_p)_b$ on the bottom

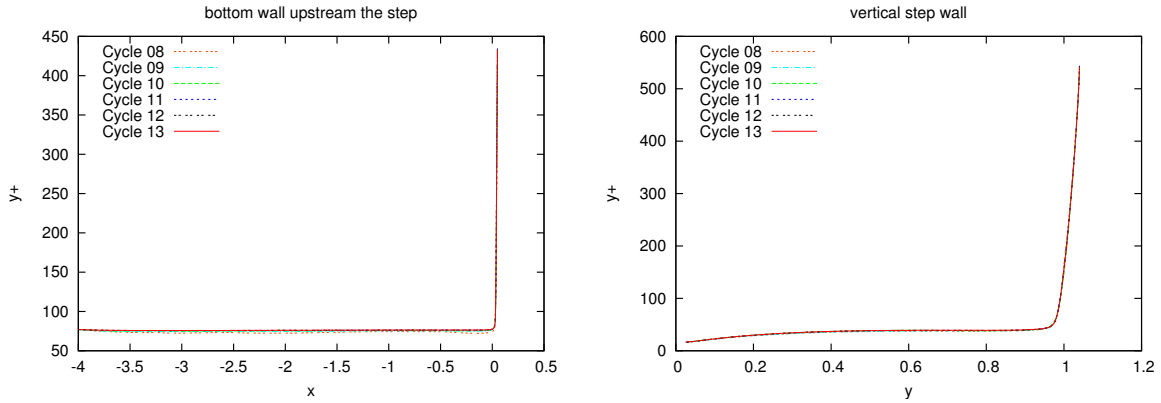

(a) (b)

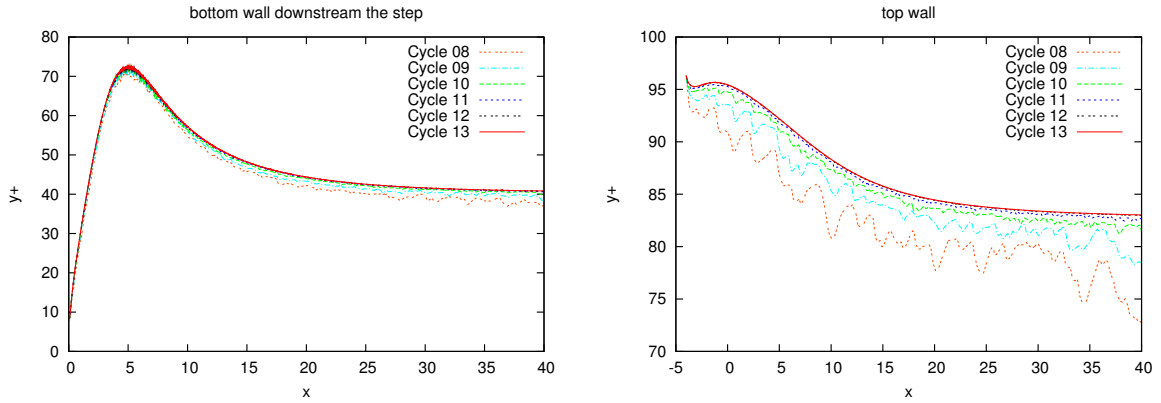

(c) (d)

Figure 16: Evolution of y_+ with adaptive cycles

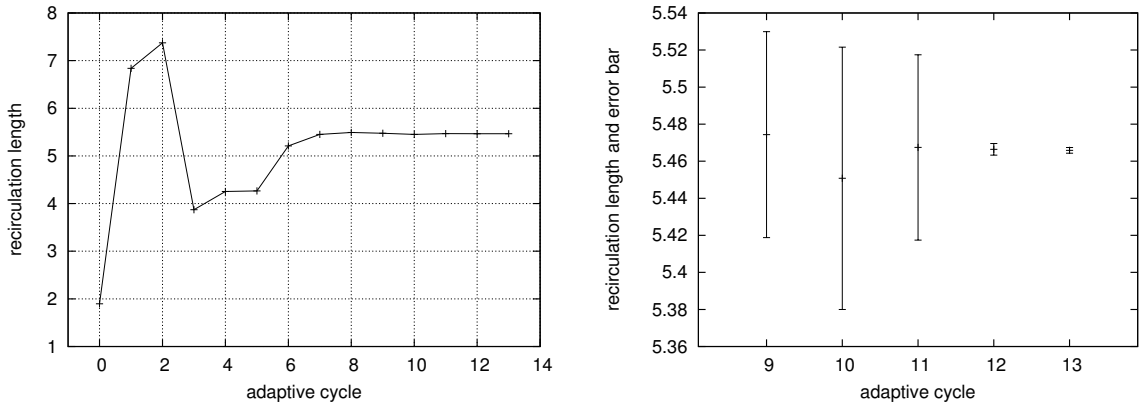

(a) Evolution with adaptive cycles

(b) Values with error bars

Figure 17: Convergence of recirculation length with adaptive cycles

wall (fig. 20). There are defined as follows :

$$(C_f)_b = \frac{1}{1/2U_{\text{ref}}^2 44H}\left[\int_{-4H}^{0}\tau_w\,dx + \int_{0}^{40H}\tau_w\,dx\right], \tag{12}$$

$$(C_f)_t = \frac{1}{1/2U_{\text{ref}}^2 44H}\left[\int_{-4H}^{40H}\tau_w\,dx\right], \tag{13}$$

$$(C_p)_b = \frac{1}{1/2U_{\text{ref}}^2 H}\int_{0}^{H} -(p-p_{\text{outlet}})|_{x=0}\,dy, \tag{14}$$

where τ_w is the skin friction. For the present geometry, given that the walls are aligned with one of the Cartesian axes, one has :

$$\tau_w = \left[(\tau\cdot\hat{\mathbf{n}})\cdot\hat{\mathbf{t}}\right]_{wall} = \left[(\nu+\nu_t)(\frac{\partial u}{\partial y}+\frac{\partial v}{\partial x})\right]_{wall} = \left[\nu\frac{\partial u}{\partial y}\right]_{wall}$$

However, in our study, the skin friction is calculated from the wall function :

$$\tau_w = \rho u_k u_{**}.$$

Note that the wall function modeling assumes that the shear stress is constant in the wall function region.

Finally, results for local flow quantities are presented. The coordinates of the three points under consideration are : Point 1 (0.0,1.1), Point 2 (1.0,0.1) and Point 3 (4.0,0.1). At these locations, we consider the mean velocity components (u and v), the pressure coefficient C_p and the eddy-viscosity ν_t. Figures 21, 22 and 23 report results for locations 1 to 3 in this order. Note that here, following the workshop instruction, the pressure coefficient is defined as :

$$C_p = \frac{p-p_{\text{outlet}}}{1/2\rho U_{\text{ref}}^2}$$

All in all, those results bring the following conclusions :

1. All quantities exhibit grid convergence with adaptive cycles. *Better and smoother* grid convergence is achieved for integral quantities than for pointwise quantities.

2. Most of pointwise quantities exhibit an oscillatory convergence. In such situations our uncertainty estimation procedure is close to the CGI practices. Indeed, for any other

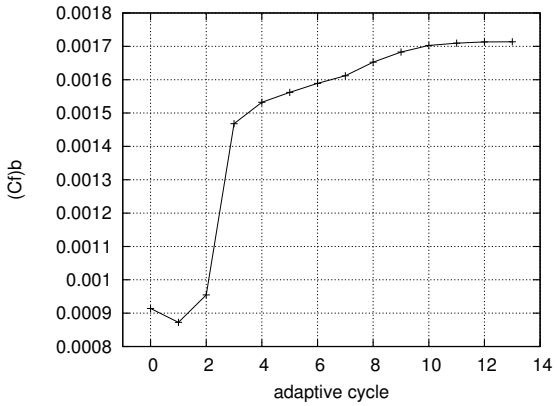

(a) Evolution with adaptive cycles

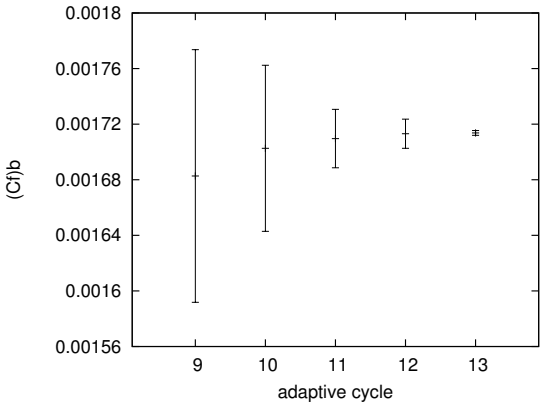

(b) Values and error bars

Figure 18: Convergence of $(C_f)_b$ with adaptive cycles

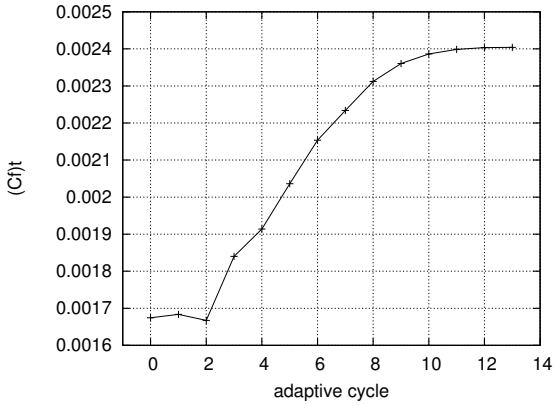

(a) Evolution with adaptive cycles

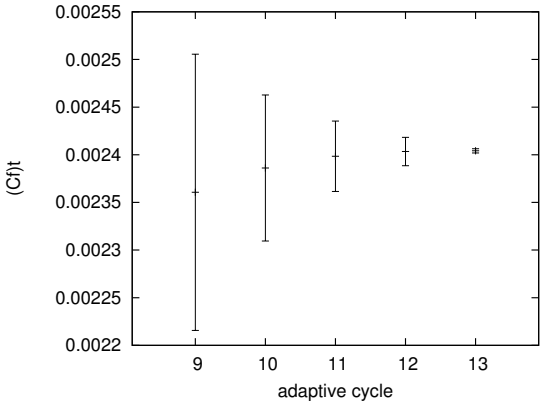

(b) Values and error bars

Figure 19: Convergence of $(C_f)_t$ with adaptive cycles

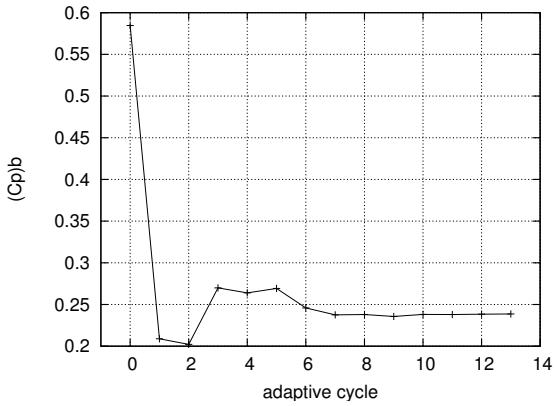

(a) Evolution with adaptive cycles

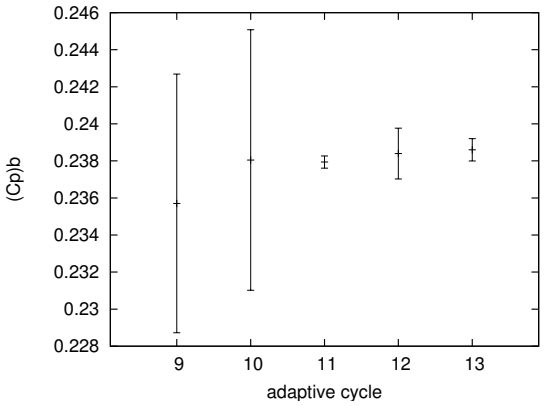

(b) Values and error bars

Figure 20: Convergence of $(C_p)_b$ with adaptive cycles

behaviors than monotonic convergence, Richardson extrapolation can not be used. In these situations, the CGI procedures use an alternative uncertainty quantification which is the maximum difference between solutions on all grids at hand with application of a factor of safety of 3.

3. In the vast majority of cases, the error bars for the *medium* grids #9 to #12 contain the predicted finest grid solutions on the last adapted mesh.

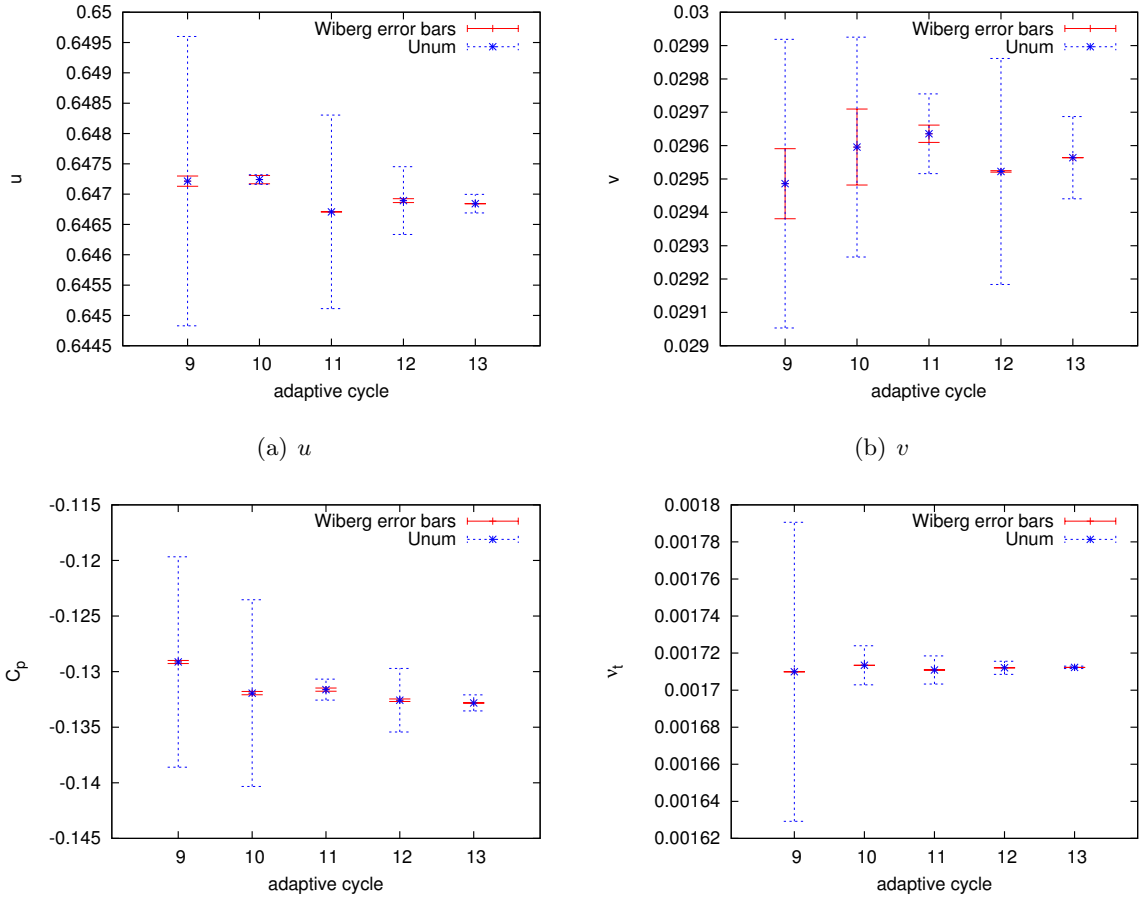

(a) u (b) v

(c) C_p (d) ν_t

Figure 21: Error bars on local quantities (point 1)

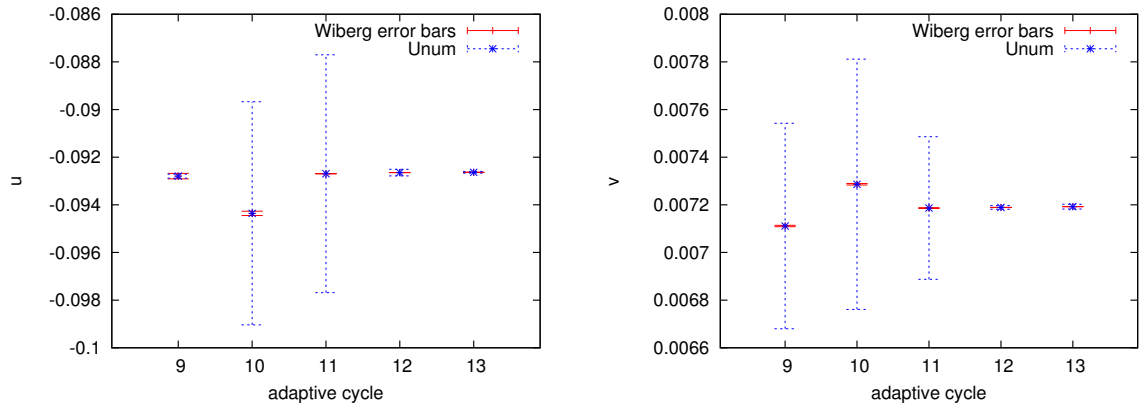

(a) u

(b) v

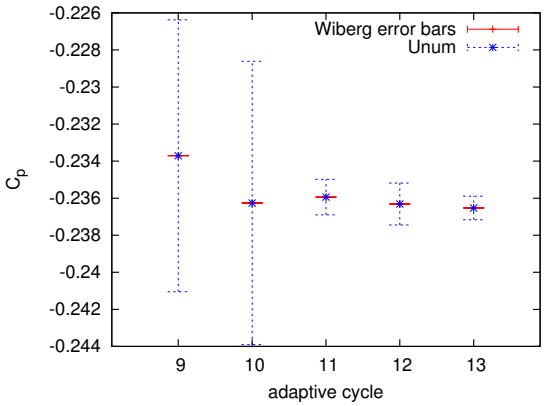

(c) C_p

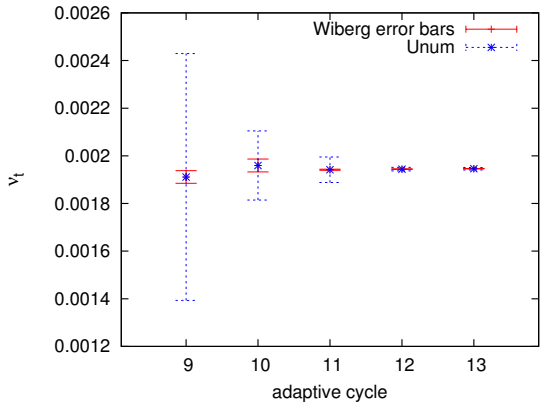

(d) ν_t

Figure 22: Error bars on local quantities (point 2)

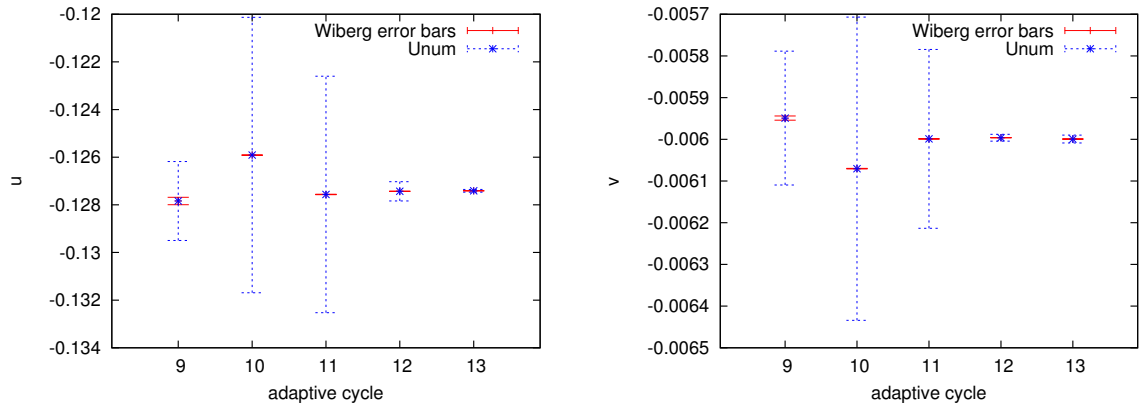

(a) u (b) v

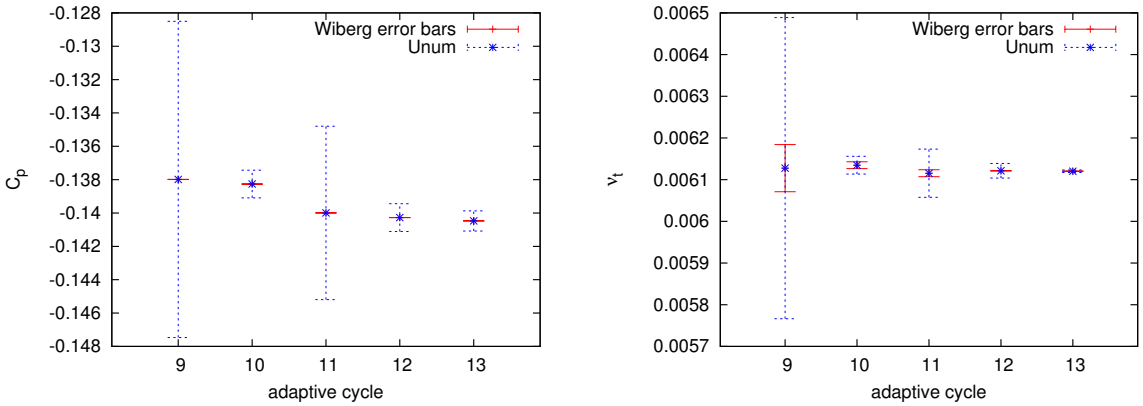

(c) C_p (d) ν_t

Figure 23: Error bars on local quantities (point 3)

6 Validation exercise for the Backward Facing Step problem

This section reports results and conclusions from the Validation exercise. The required validation procedure is adapted from the ASME/ANSI Standard document [25] which uses internationally accepted concepts of uncertainty defined in Ref. [26]. The procedure has been summed up in the workshop instruction for the convenience of participants and will not be reproduced here. In what follows, we use the *strong model* concept that assumes fixed parameters meaning that their is no uncertainty in the problem parameters ($U_{\text{input}} = 0$) (boundary conditions, geometry representation, etc).

S	U_{num}	U_{input}	D	U_D	E	U_{val}
5.46588	0.00153	0.0000	6.26	0.10	-0.79412	0.10001

Table 5: Validation exercise for the recirculation length

The results for the recirculation length are given in table 5. The agreement between the numerical result and the experimental data is relatively poor so that the absolute value of the validation comparison error E is large. Given that the numerical uncertainty predicted U_{num} is very small, the validation uncertainty U_{val} equals the experimental uncertainty U_D. However, $|E| >> U_{\text{val}}$ so that the modeling error is of the order of the validation comparison error. Hence, numerical simulations could be used to test changes in the model (*RANSE + standard* $k-\epsilon$ *+ wall functions*) aiming at reducing the modeling error. Furthermore, these modeling improvements are strongly needed. Indeed, $|E|$ is large compared to S so that our model is relatively poor. This was expected since the standard $k-\epsilon$ turbulence model is widely known to badly predict reattachment points. It gets worse in the presence of adverse pressure gradients. This is one of the main limitations of the first-order $k-\epsilon$ family of turbulence models.

We now apply the validation procedure to pressure and friction distributions along walls. Figures 24, 25 and 26 present the results for the pressure coefficient along the bottom wall, the pressure coefficient along the top wall and the friction coefficient along the bottom wall respectively. In each case, figure (a) shows the comparison between the numerical predictions and the experimental measurements with their associated uncertainty bars. Figure (b) shows the distribution of the validation comparison error with the validation uncertainty as error bars. As can be seen, the agreement between numerics and experiments is fairly good except in the area directly downstream of the corner step. Again, the numerical uncertainty is extremely small compared to both the solution magnitude and the experimental uncertainty. As a general trend, the numerical predictions are within the experimental uncertainties so that the validation uncertainty error is mostly of the same order than the validation uncertainty. Hence, the modeling error is within the *noise level* from all the other source of uncertainties (here mainly the experimental uncertainty) so that modeling improvements would be difficult. This trend is not closely observed in the region nearby the step where thus some improvements may be potentially achieved.

Finally, we consider local flow quantities extracted along transversal cuts normal to the walls. Figures 27, 28 and 29 show profiles extracted at $x/H = 1$ for the streamwise component of the velocity, the normal component of the velocity and the Reynolds shear stress respectively. Figures (a) and (b) present the same results as previously. Following this pre-

sentation pattern, profiles are also extracted at $x/H = 4$ in figures 30 to 32, and at $x/H = 6$ in figures 33 to 35.
Generally speaking, the numerical predictions of the streamwise velocity component agree well with the experiments. It looses accuracy in the near wall region of the recirculating zone (this is due to the wall functions modeling). The level of shear stress from the turbulent fluctuations is also fairly well approximated given that it is a quantity which is not easily modeled. The poorest numerical predictions are observed for the y-component of the velocity which is largely under-predicted even around the mid-line of the channel.
Interpretation of the validation results indicate that few improvements can be expected outside of the recirculation area except for the normal velocity component. In the recirculating region however, $|E| >> U_{\text{val}}$. Here, our model could be largely improved and numerical simulations could help assessing if substantial improvements are achieved.

7 Concluding remarks

This paper has presented the results of the workshop activities which provided a complete set of exercises with respect to Verification and Validation since Code Verification, Solution Verification and Solution Validation were all included. The required exercises were performed using an adaptive finite-element solver based on RANS equations, the standard $k - \epsilon$ model of turbulence and a two-velocity scale wall functions. In our approach, adaptivity is driven by the ZZ error estimator which provides error estimates measured in elemental error norms. Aside from driving the adaptive procedure, it allows for the calculation of the observed order of convergence in solution variables but can not yield pointwise error estimations. We have shown how an L_2 least-squares approach can provide such local error estimations. Furthermore, we have introduced an uncertainty prediction procedure which largely relies on the grid adaptive procedure. This adaptivity-based uncertainty estimator brings error bars at no extra cost since the adaptive procedure is already used to yield grid-independent solution predictions.

Results from Code Verification by the MMS have shown that the flow solver, the adaptive procedure and the ZZ error estimator have all been verified in the context of turbulent flows with wall functions. We also have taken advantage of the opportunity offered by the availability of true errors to access error estimators and the uncertainty prediction procedure. Estimated error norms from the ZZ estimator show almost asymptotic exactness. The Wiberg estimator for pointwise error estimations only predicts the order of magnitude of true errors. They usually both under-predict the true error and can not thus directly provide reliable error bars. However, the adaptivity-based uncertainty estimation procedure has been shown to achieve the required 95% certainty level of confidence. It is thus on par with the GCI procedures but demands no user-intervention or additional computational efforts. Obviously, further testing on a statistically significant number of cases is needed to confirm these favorable results given that the factor of safety is an ad-hoc choice based on limited previous experiences and do not rely on solid theoretical ground.

Results from Solution Verification have shown that the adaptive procedure automatically yield grid-converged numerical predictions in the asymptotic range (as long as enough computer resources are available). Also, the error bars for the numerical predictions on the middle grids in the adaptive process have been shown to contain the finest grid solution which is another encouraging result for adaptivity-based uncertainty estimator.

Results from the Validation exercises have shown that the main source of uncertainty in the numerical predictions comes from the modeling error. The interpretation of the Validation results has successfully highlighted which parts of the numerical predictions would clearly benefit modeling improvements and whether or not these improvements are possible based on CFD. Those results agree well with the well-known limitations of both the $k - \epsilon$ model and the use of wall functions.

8 Acknowledgments

As it may be the last workshop on CFD Uncertainty Analysis held in Lisbon, the authors would like to congratulate and thank Prof. Luís Eça and Martin Hoekstra for all the work they have done to successfully think, prepare and organized these three workshops. We believe that, as we have, all participants and the V&V discipline has gained from the open discussions and interesting conclusions drawn during these events.
Also, we have had a wonderful and friendly time in Lisbon.

References

[1] P. J. Roache. *Verification and Validation in Computational Science and Engineering*. Hermosa Publishers, Albuquerque, NM, 1998.

[2] P. J. Roache. Code Verification by the Method of Manufactured Solutions. *ASME Journal of Fluids Engineering*, 114(1):4–10, 2002.

[3] A. Hay and D. Pelletier. Code and solution verification of an adaptive finite element turbulent flow solver. In *18th AIAA Computational Fluid Dynamics Conference*, Miami, FL, June 2007. AIAA-2007-4202.

[4] A. Hay, S. Etienne, and D. Pelletier. Adaptivity, sensitivities and uncertainties in cfd. In *AVT Symposium on "Computational Uncertainty in Military Vehicle Design*, Athens, Greece, December 2007.

[5] F. Ilinca and D. Pelletier. Positivity preservation and adaptive solution for the $k - \epsilon$ model of turbulence. *AIAA Journal*, 36(1):44–51, 1998.

[6] J.-P. Chabard. Projet N3S - manuel de la version 3, 1991. Tech. Rep. EDF HE-41/91.30B, Electricité de France.

[7] A. N. Brooks and T. J. R. Hughes. Streamline upwind/petrov-galerkin formulations for convection dominated flows with particular emphasis on the incompressible navier-stokes equations. *Computer Methods in Applied Mechanics and Engineering*, 32:199–259, 1982.

[8] F. Ilinca, J.-F. Hétu, and D. Pelletier. On stabilized finite element formulations for incompressible advective-diffusive transport and fluid flow problems. *Computer Methods in Applied Mechanics and Engineering*, 188(1):235–257, 2000.

[9] UMFPACK. Copyright (c) 1994-2007 by Timothy A. Davis, University of Florida. All Rights Reserved. Distributed under the GNU GPL license. http://www.cise.ufl.edu/research/sparse/umfpack/.

[10] F. Ilinca, J.-F. Hétu, and D. Pelletier. Adaptive remeshing for the $k - \epsilon$ model of turbulence. *Computers and Fluids*, 27(3):291–310, 1998.

[11] F. Ilinca and J.-F. Hétu. Finite element solution of three-dimensional turbulent flowsapplied to mold-filling problems. *International Journal for Numerical Methods in Fluids*, 34:729–750, 2000.

[12] O. C. Zienkiewicz and J. Z. Zhu. The superconvergent patch recovery and *a posteriori* error estimates. Part 1: The recovery technique. *International Journal for Numerical Methods in Engineering*, 33:1331–1364, 1992.

[13] O. C. Zienkiewicz and J. Z. Zhu. The superconvergent patch recovery and *a posteriori* error estimates. Part 2: Error estimates and adaptivity. *International Journal for Numerical Methods in Engineering*, 33:1365–1382, 1992.

[14] J. Peraire, M. Vahdati, K. Morgan, and O.C. Ziekiewicz. Adaptive remeshing for compressible flow computations. *Journal of Computational Physics*, 72(2):449–466, 1987.

[15] D. Pelletier. Adaptive finite element computations of complex flows. *International Journal for Numerical Methods in Fluids*, 31:189–202, 1999.

[16] D. Pelletier and F. Ilinca. Adaptive remeshing for the $k - \epsilon$ model of turbulence. *AIAA Journal*, 35(4):640–646, 1997.

[17] X. D. Li and N.-E. Wiberg. A posteriori error estimate by element patch post-processing, adaptive analysis in energy and l_2 norms. *Computers and Structures*, 53(4):907–919, 1994.

[18] L. Eça and M. Hoekstra. An evaluation of verification procedurres for cfd applications. In *24th Symposium on Naval Hydrodynamics*, Fukuoka, Japan, July 2002.

[19] L. Eça and M. Hoekstra. Discretization uncertainty estimation based on a least squares version of the grid convergence index. In *2nd Workshop on CFD Uncertainty Analysis*, Lisbon, Portugal, October 2006.

[20] P. Roache and D. Pelletier. Verification and validation of computational heat transfer. In W. J. Minkowycz, E. M. Sparrow, and J. Y. Murthy, editors, *Handbook of Numerical Heat Transfert, Second Edition*, chapter 13, pages 417–437. John Wiley & Sons, Inc., Hoboken, New Jersey, 2006.

[21] E. Turgeon, D. Pelletier, and L. Ignat. Effects of adaptivity on finite element schemes for turbulent heat transfert and flow predictions. *Numerical Heat Transfert, Part A*, 38:847–686, 2000.

[22] D. Pelletier and P. J. Roache. CFD code Verification and the Method of the Manufactured Solutions. In *10th Annual Conference of the CFD Society of Canada*, Windsor, Ontario, Canada, June 2002.

[23] L. Eça, M. Hoekstra, A. Hay, and D. Pelletier. A manufactured solution for a two-dimensional steady wall-bounded incompressible turbulent flow. *International Journal of Computational Fluid Dynamics*, 21(3-4):175–188, 2007.

[24] L. Eça, M. Hoekstra, A. Hay, and D. Pelletier. Verification of RANS solvers with manufactured solutions. *Engineering with computers*, 23:253–270, 2007.

[25] ASME V&V 20-2008. Standard for Verification and Validation in Computational Fluid Dynamics and Heat Transfert, expected 2008. ASME Committee PTC 61.

[26] ASME PTC 19.1-2005. *Test Uncertainty*. ASME, New-York, 2006.

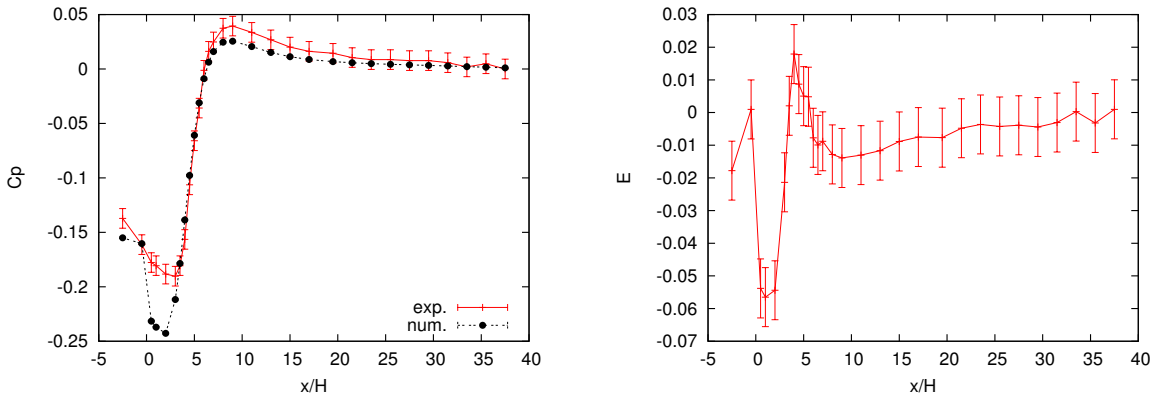

(a) $D \pm U_D(\text{exp.})$ and $S \pm U_{\text{num}}(\text{exp.})$ (b) $E \pm U_{\text{val}}$

Figure 24: Pressure coefficient along the bottom wall

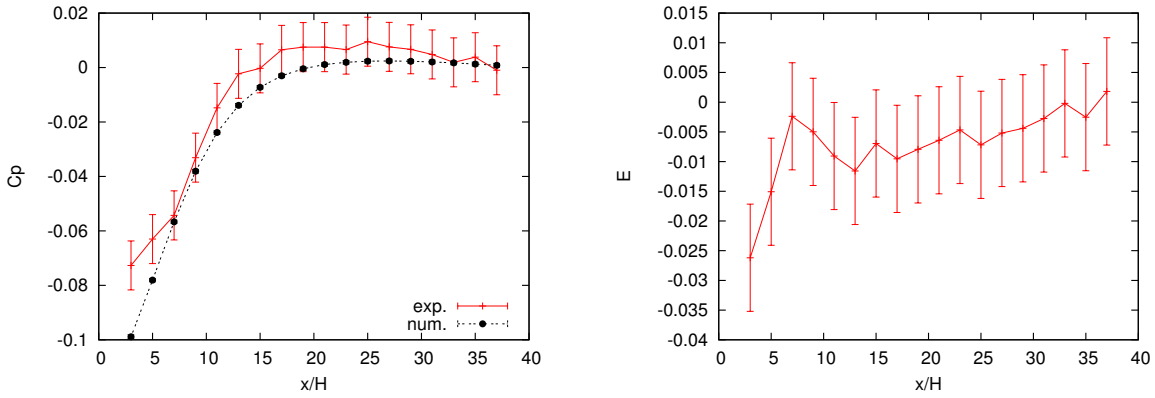

(a) $D \pm U_D(\text{exp.})$ and $S \pm U_{\text{num}}(\text{exp.})$ (b) $E \pm U_{\text{val}}$

Figure 25: Pressure coefficient along the top wall

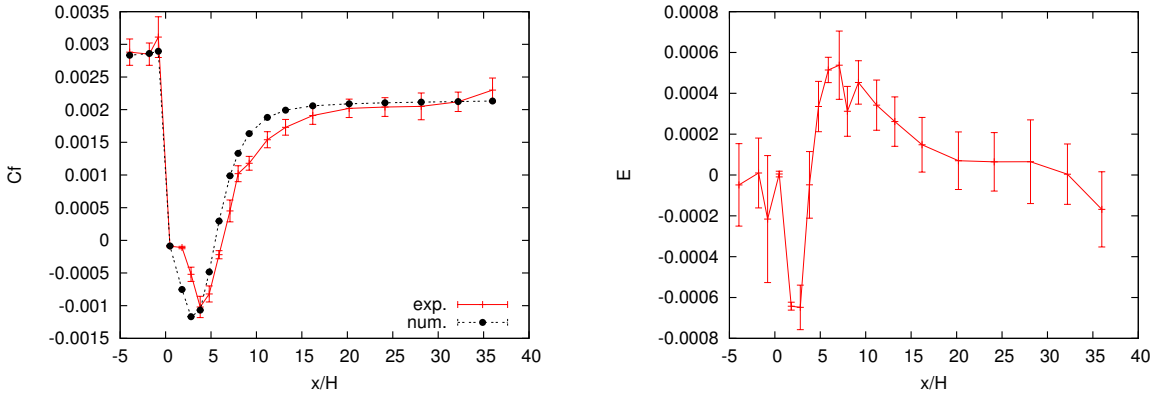

(a) $D \pm U_D(\text{exp.})$ and $S \pm U_{\text{num}}(\text{exp.})$ (b) $E \pm U_{\text{val}}$

Figure 26: Skin friction coefficient along the bottom wall

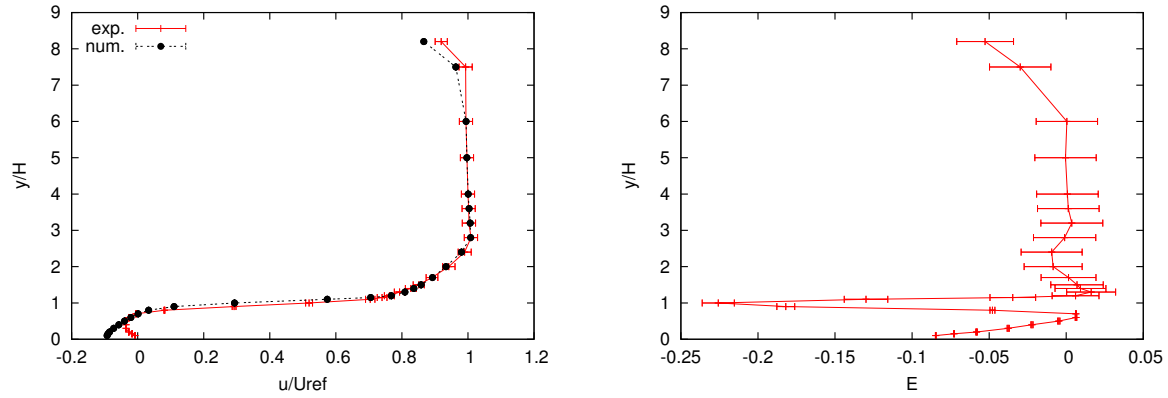

(a) $D \pm U_D(\text{exp.})$ and $S \pm U_{\text{num}}(\text{exp.})$ (b) $E \pm U_{\text{val}}$

Figure 27: u/U_{ref} at $x/H = 1$

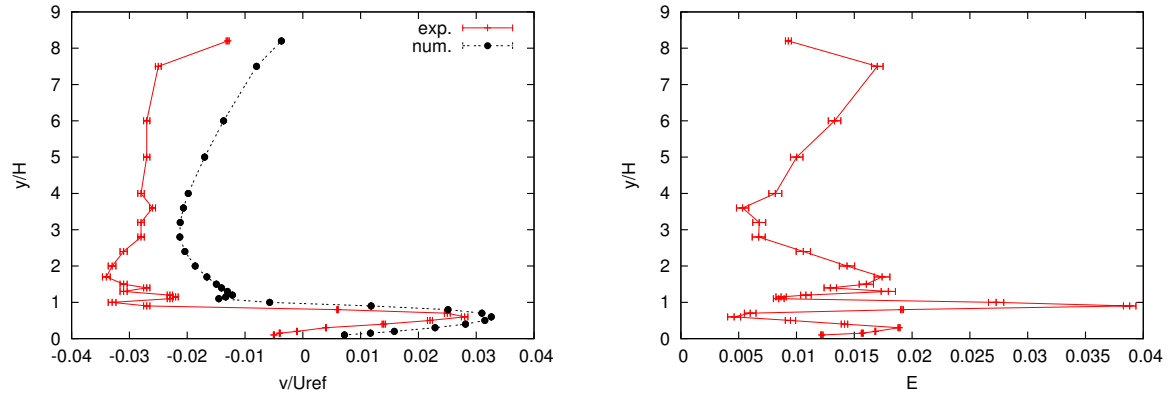

(a) $D \pm U_D(\text{exp.})$ and $S \pm U_{\text{num}}(\text{exp.})$ (b) $E \pm U_{\text{val}}$

Figure 28: v/U_{ref} at $x/H = 1$

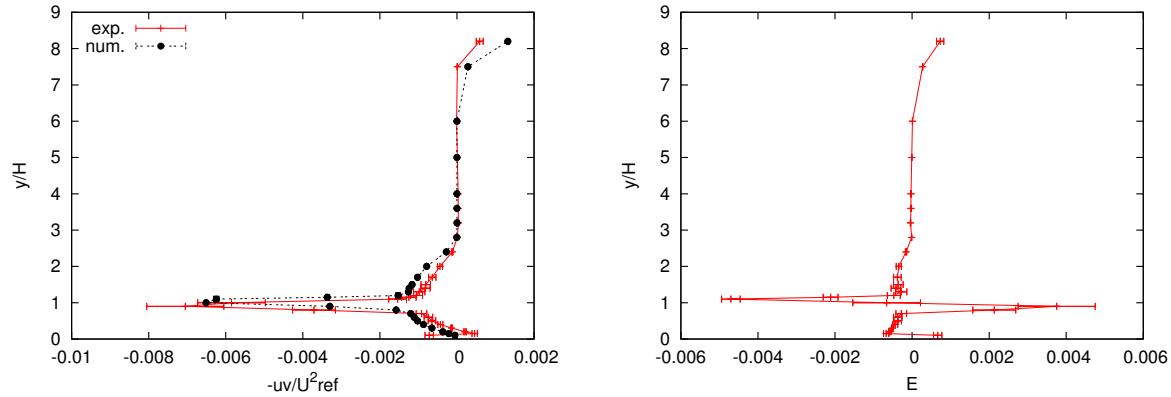

(a) $D \pm U_D(\text{exp.})$ and $S \pm U_{\text{num}}(\text{exp.})$ (b) $E \pm U_{\text{val}}$

Figure 29: $-\overline{u'v'}/U^2_{ref}$ at $x/H = 1$

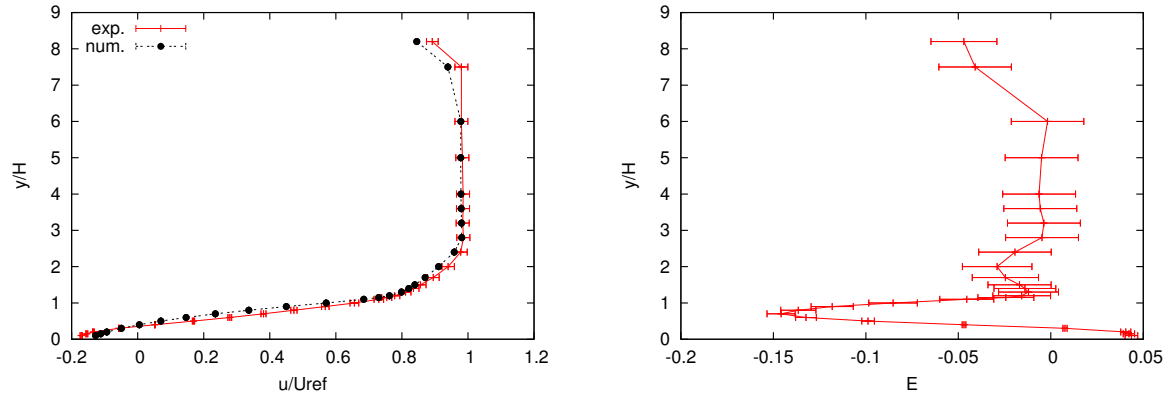

(a) $D \pm U_D(\text{exp.})$ and $S \pm U_{\text{num}}(\text{exp.})$ (b) $E \pm U_{\text{val}}$

Figure 30: u/U_{ref} at $x/H = 4$

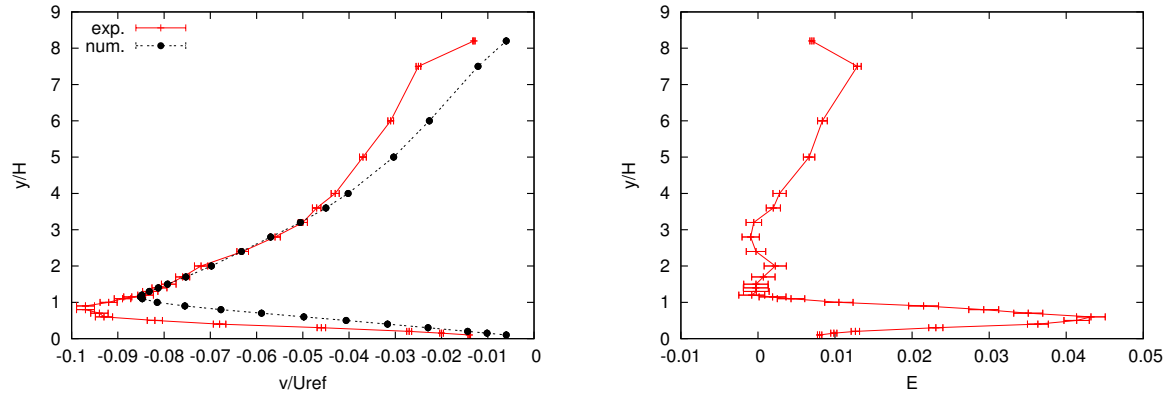

(a) $D \pm U_D(\text{exp.})$ and $S \pm U_{\text{num}}(\text{exp.})$ (b) $E \pm U_{\text{val}}$

Figure 31: v/U_{ref} at $x/H = 4$

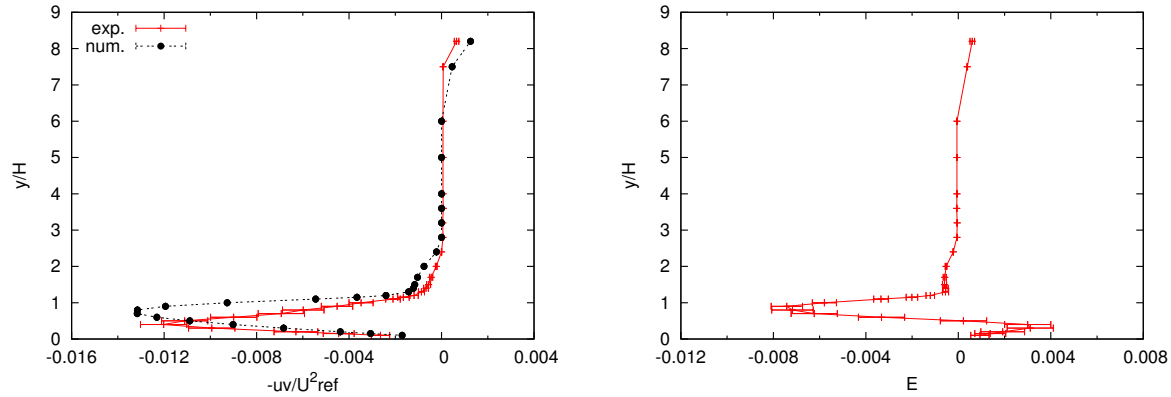

(a) $D \pm U_D(\text{exp.})$ and $S \pm U_{\text{num}}(\text{exp.})$ (b) $E \pm U_{\text{val}}$

Figure 32: $-\overline{u'v'}/U_{ref}^2$ at $x/H = 4$

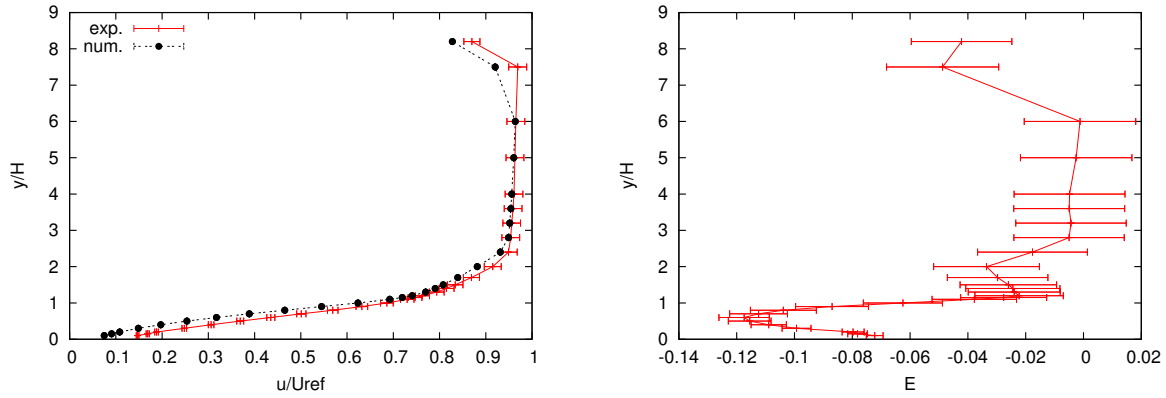

(a) $D \pm U_D(\text{exp.})$ and $S \pm U_{\text{num}}(\text{exp.})$ (b) $E \pm U_{\text{val}}$

Figure 33: u/U_{ref} at $x/H = 6$

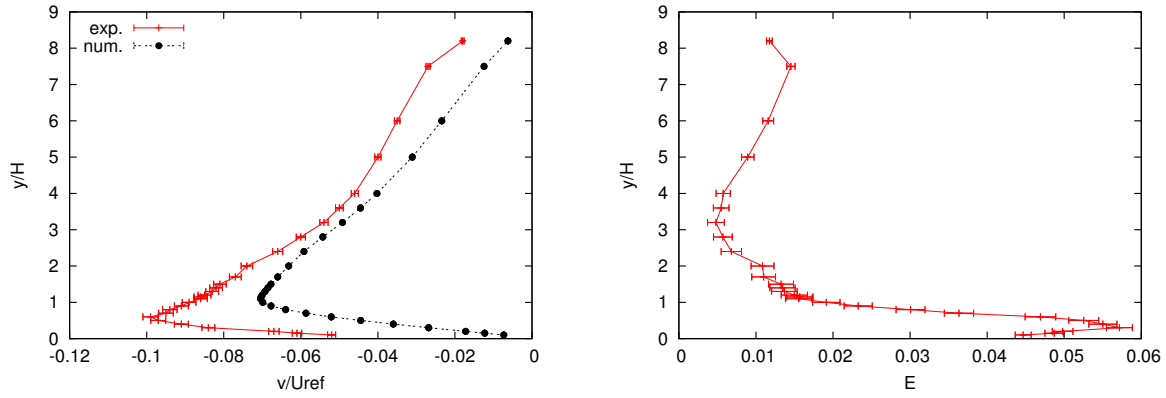

(a) $D \pm U_D(\text{exp.})$ and $S \pm U_{\text{num}}(\text{exp.})$ (b) $E \pm U_{\text{val}}$

Figure 34: v/U_{ref} at $x/H = 6$

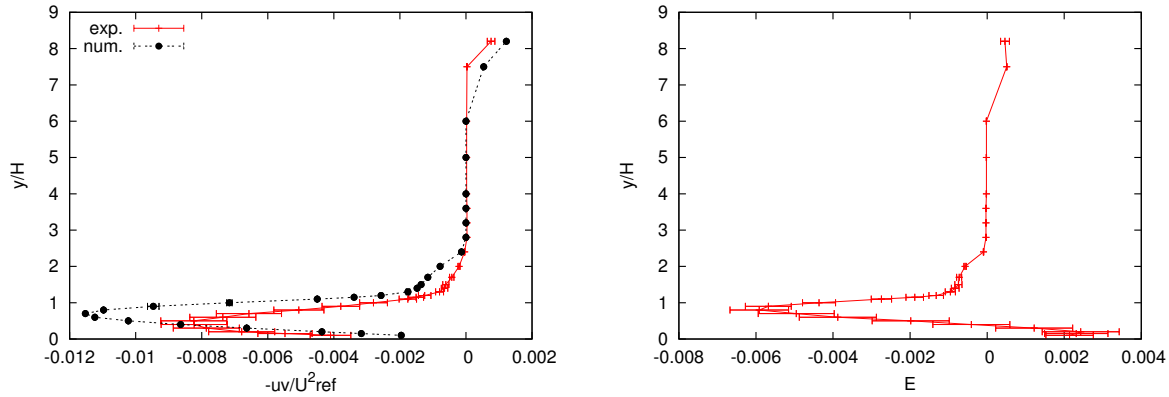

(a) $D \pm U_D(\text{exp.})$ and $S \pm U_{\text{num}}(\text{exp.})$ (b) $E \pm U_{\text{val}}$

Figure 35: $-\overline{u'v'}/U_{ref}^2$ at $x/H = 6$